RESEARCH ARTICLE

ADVANCED HEALTHCARE MATERIALS
www.advhealthmat.de

Engineering a Human-Sized Common Bile Duct Prototype with Regenerative Potential: In Vitro Evaluation of Mechanics, Function, Degradation, and Immune Modulation

Mattia Pasqua, Marianna Barbuto, Matteo Calligaris, Roberto Di Gesù, Duilio Pagano, Rosalia Busà, Salvatore Gruttadauria, Simone Dario Scilabra, Antonio D'Amore, and Maria Giovanna Francipane**

Tissue engineering offers new hope for treating biliary defects. Several scaffolds have been proposed, but their properties have not been fully investigated. In this study, the design, fabrication, and characterization of a novel common bile duct (CBD)-like prototype are described. This prototype combines two biocompatible biomaterials, methacrylated type I collagen (CollMA) and poly(ϵ-caprolactone) (PCL), along with biliary epithelial cells. CollMA supports the organization of biliary epithelial cells into a functional biliary-like epithelium, as shown by histological, functional, and proteomic assays, while PCL provides mechanical strength. The biological and mechanical phases of the prototype are integrated into a multiphasic tubular scaffold using molding and electrospinning techniques. The final CBD-like prototype consists of three interpenetrating phases: from innermost to outermost, these are biliary epithelial cell-laden CollMA, PCL, and CollMA. This design overcomes challenges seen in multilayer constructs, such as interlayer delamination and lack of homogeneity. The prototype remains stable under physiological conditions, enables bile flow without leakage, and exhibits bile acid transport and modification activities, warranting future in vivo preclinical evaluation. In an ex vivo human blood assay, the acellular prototype elicited a favorable immune response, limiting inflammation and promoting sustained release of epidermal growth factor (EGF), indicating its potential to support regenerative processes.

1. Introduction

The biliary tree is a complex network of ducts responsible for transporting, modifying, storing, and secreting bile into the intestine during digestion. Narrowing or obstruction of any bile duct, known as stenosis or stricture, disrupts bile flow, leading to cholestasis and the accumulation of bile in the liver. Biliary strictures can result from various etiologies, including surgical injuries (e.g., laparoscopic cholecystectomy), inflammation, tumors, and other conditions. If untreated, this can impair liver function to the point where a liver transplant becomes necessary.[1] Liver transplants can themselves lead to strictures and complications such as bile loss and external biliary fistulas, where bile flows through abnormal connections between a bile duct and a nearby hollow structure. The use of livers from donors after cardiac death is associated with the highest complication rates.[2] As this practice becomes more common in European countries, including Italy,[3] effective strategies for preventing and treating postoperative

M. Pasqua, M. Barbuto, M. Calligaris, R. Di Gesù, S. D. Scilabra, A. D'Amore, M. G. Francipane
Ri.MED Foundation
Palermo 90133, Italy
E-mail: mpasqua@fondazionerimed.com; mgfrancipane@fondazionerimed.com

The ORCID identification number(s) for the author(s) of this article can be found under https://doi.org/10.1002/adhm.202501660

DOI: 10.1002/adhm.202501660

M. Barbuto
Department of Biological
Chemical and Pharmaceutical Sciences and Technologies (STeBiCeF)
University of Palermo
Palermo 90128, Italy

M. Barbuto, A. D'Amore, M. G. Francipane
McGowan Institute for Regenerative Medicine
University of Pittsburgh
Pittsburgh, PA 15219, USA

D. Pagano, S. Gruttadauria
Abdominal Center
UPMC
Palermo 90127, Italy

R. Busà
Research Department
IRCCS ISMETT
Palermo 90127, Italy

complications, especially the insidious ischemic non-anastomotic strictures,[4] are essential.

Endoscopic retrograde cholangiopancreatography is the gold standard for diagnosing biliary duct disorders and is commonly used alongside biliary stenting as the first-line treatment for benign biliary strictures.[5] Plastic stents, available in various types,[6] are used to expand the diameter of strictures caused by liver transplantation, chronic pancreatitis, or cholecystectomy, with placement recommended at three-month intervals for at least a year, according to the 2018 European Society of Gastrointestinal Endoscopy guidelines.[7] While this protocol resolves most strictures temporarily (85%–90%), recurrences occur in 5%–20% of cases,[8] requiring repeated endoscopic procedures that increase the risk of bleeding, infections, pancreatitis, and intestinal perforation, as well as placing a burden on healthcare systems.[9]

To reduce the number of required procedures, self-expanding metal stents (SEMS) have become more widely used over the last decade.[6] There are three types of SEMS: uncovered (USEMS), partially covered, and fully covered (FCSEMS).[5] USEMS are unsuitable for benign biliary strictures due to their non-removability once hyperplastic growth occurs.[10] FCSEMS, increasingly approved for benign stricture treatment, have demonstrated comparable effectiveness to plastic stents and can sometimes replace multiple plastic stents, especially in cases related to chronic pancreatitis or cholecystectomy.[7] However, long-term use of FCSEMS carries a higher risk of migration.[11]

Stent selection ultimately depends on factors such as stricture length, location, cause, patient prognosis, healthcare costs, and surgeon experience. In complex or recurrent cases, percutaneous interventions and surgical procedures like biliary-enteric anastomosis remain preferred options,[5] though they also carry potential complications.[12,13]

As treatment options for biliary complications evolve, research is increasingly focused on biodegradable polymeric scaffolds[14] that support tissue regeneration while gradually resorbing within the host, eliminating the need for repeated placement or removal. A key challenge, however, is balancing the degradation rate of the scaffold with the pace of tissue regeneration. Upon implantation, the scaffold is expected to initiate a three-stage wound healing process: 1) early immune cell infiltration and recruitment of regenerative cells; 2) secretion of extracellular matrix; and 3) regeneration of functional, native-like tissue. The scaffold should degrade over time to prevent chronic inflammation and scarring, while allowing new tissue to restore structural integrity.

To meet these demands, a range of synthetic and natural biomaterials have been explored, from non-degradable materials like polytetrafluoroethylene (Teflon) to biodegradable polymers such as polyglycolic acid, poly(ϵ-caprolactone) (PCL), and collagen.[15–21] These scaffolds have been used either alone or in combination with cells or host tissues such as the greater omentum,[22] small intestine submucosa,[23] or ureter[24] to improve integration and tissue remodeling.

While cell-free approaches bypass the need for donor cells, they may be less effective in patients with impaired in situ regenerative capacity. In contrast, ex vivo tissue engineering, combining biomaterials with cells in vitro, offers the potential to create more biologically relevant constructs that better mimic native tissue function.[16] Various cell sources have been investigated, including bone marrow cells,[25–27] liver stem cell-derived biliary epithelial-like cells,[28,29] and human primary biliary epithelial cells.[30] Despite encouraging results, these strategies remain poorly translatable to clinical practice.

Balancing simplicity and effectiveness in biliary duct tissue engineering remains challenging. Many earlier approaches focused on chemical and mechanical properties of biomaterials, often overlooking the complex, multilayered, and dynamic nature of biliary ducts. The human common bile duct (CBD), for example, is a small tube (≈6 cm long, <6 mm in diameter),[31] composed of an epithelial layer, submucosa, and an outer collagenous layer.[32] The epithelial lining, made up of biliary epithelial cells (cholangiocytes), contains multiple transporters, channels, and exchangers on both apical and basolateral membranes, enabling bile modification through secretion and absorption processes.[33] The CBD is also vascularized by arteries and veins, though the exact vascular architecture remains poorly defined.[34]

Building on knowledge of CBD anatomy, physiology, and mechanics, we designed, fabricated, and characterized a functional CBD-like prototype that integrates two biocompatible biomaterials, methacrylated type I collagen (CollMA) and PCL, with biliary epithelial cells.

An electrospun PCL (ES-PCL) tubular scaffold was first fabricated using electrospinning and then encapsulated between two layers of CollMA via molding: an inner, cell-laden layer and an outer, and cell-free layer. The inner layer developed into a functional biliary-like epithelium, while the outer layer is intended to provide a favorable interface for host integration following implantation. The central PCL scaffold imparts essential mechanical strength. This design effectively addresses common issues of interlayer delamination and structural inhomogeneity.[26]

The prototype resists degradation under physiologically relevant conditions, enables bile flow without leakage, and demonstrates bile acid transport and modification activities. Furthermore, in an ex vivo human blood assay, the prototype's biomaterials elicited a favorable immune response, promoting sustained release of epidermal growth factor (EGF) and preventing excessive inflammation. These promising results suggest that the prototype may support tissue repair and integration, warranting further preclinical in vivo evaluation.

2. Results

2.1. Feasibility of Our Biofabrication Approach for the Generation of a CBD-Like Construct

Bile duct tissue engineering faces significant challenges in assembling cells and biomaterials into a biocompatible tubular structure that mimics both the architecture and function of native tissue.

S. Gruttadauria
Department of General Surgery and Medical-Surgical Specialties
University of Catania
Catania 95124, Italy

A. D'Amore
Departments of Surgery and Bioengineering
University of Pittsburgh
Pittsburgh, PA 15213, USA

For our CBD-like construct, we used two biomaterials: CollMA and PCL. Collagen, a major constituent of the CBD's extracellular matrix (ECM),[35] offers ideal support for biliary epithelial cells, while PCL, a biocompatible synthetic polymer, provides essential mechanical properties, such as ductility, stability, and impact resistance,[36] along with biodegradability and bioresorbability.[15,37]

Our approach involves fabricating an electrospun (ES) PCL tubular scaffold (mechanical phase) and combining it with a biliary epithelial cell-laden CollMA solution (biological phase) on the inner side and a cell-free CollMA solution on the outer side, using a mold. This method, illustrated in **Figure 1**a,c$_1$ and Video S1 (Supporting Information), was initially validated using biomaterials alone, resulting in a stable, multiphasic tubular structure. Our construct replicates the average human CBD dimensions (6 cm length, 1–2 mm thickness),[31,38,39] with the flexibility to adjust the size by varying the length of the ES-PCL scaffold and the amount of CollMA solution.

Scanning electron microscopy (SEM) analysis confirmed the interpenetration of CollMA into the PCL fibers (Figure 1c,2–4) and demonstrated homogeneity. No delamination between the polymer layers occurred during a 14-day incubation in the medium, with the layers remaining firmly adhered throughout (Figure 1c,5). In contrast, a bilayer construct comprising a single CollMA layer on the inner side of the ES-PCL scaffold showed poor stability and frequent delamination, especially during handling (data not shown). Therefore, encapsulating the ES-PCL between two layers of CollMA greatly improved structural integrity and cohesion.

After confirming the feasibility of this biofabrication method, we focused on two main activities: 1) characterizing the PCL-based mechanical phase and 2) regenerating a functional biliary-like epithelium.

2.2. The PCL-Based Mechanical Phase of Our CBD-Like Construct Possesses Acceptable Stiffness and Suturability

For implantation, tissue-engineered constructs must exhibit adequate mechanical properties, including handleability and suturability. As mentioned earlier, we selected PCL for this purpose.

The ES-PCL tubular scaffold, which we fabricated using electrospinning, had an average wall thickness of 0.18 ± 0.06 mm (data not shown). The fibers were randomly oriented (**Figure 2**a), with an average diameter of 0.53 ± 0.09 µm (data not shown), forming a porous architecture that supported cell infiltration (data not shown).

To assess performance, specifically resistance to lengthwise tension (Young's Modulus, *E*), we conducted uniaxial tensile tests on ES-PCL scaffolds, cell-free and cellularized CBD-like constructs (details on cellularization below), and native porcine CBDs, used as controls due to their anatomical similarity to human ducts, which were unavailable.[40] The ES-PCL and cell-free constructs showed comparable Young's modulus values (Figure 2b), indicating that PCL largely determines the construct's mechanical behavior. In contrast, the cellularized construct had significantly lower stiffness than the cell-free version ($p < 0.01$), with values closer to those of native ducts ($p < 0.05$). This softening is likely due to cell-driven matrix remodeling or scaffold degradation, suggesting a more biologically relevant mechanical profile.

The ES-PCL tubular scaffold also showed good suturability, with an average suture retention strength of 1.6 ± 0.5 N (Figure 2c), in line with reported values[41] and approaching the 2 N minimum typically required for small-diameter grafts.[42]

2.3. The CBD-Like Construct Enables Bile Flow Without Leakage

Preventing bile leakage is essential for any tissue-engineered CBD. We evaluated the bile permeability of both the ES-PCL scaffold and the cell-free CBD-like construct using a custom-made perfusion system (Figure 2d, left). The ES-PCL scaffold showed an average leakage rate of 6 ± 1% (Figure 2d, right). In contrast, the cell-free CBD-like construct exhibited no leakage, either immediately after fabrication (Figure 2d, right) or after 14 days in culture (not shown). This is clinically relevant, as bile leakage is a major limitation of artificial CBD devices,[16] and poses toxicity risks to surrounding tissues.

2.4. The CollMA Tubular Scaffold Degrades in Bile within 35 days, while the ES-PCL Tubular Scaffold Remains Intact for a Longer Time

A tissue-engineered CBD should degrade at a rate compatible with tissue regeneration. We therefore evaluated the degradation of the ES-PCL scaffold, CollMA scaffold, and cell-free CBD-like construct in bile and PBS using a weight-loss method. After initial swelling within the first hour (data not shown), the ES-PCL scaffold maintained stable weight with no significant differences between bile and PBS up to Day 63 (Figure 2e), showing high resistance. In contrast, the CollMA scaffold degraded progressively in bile but remained stable in PBS (Figure 2f). By Day 21, it lost 61 ± 5% of its initial weight in bile ($p < 0.0001$), with complete degradation occurring between Days 28 and 35. The cell-free CBD-like construct showed intermediate behavior (Figure 2g), losing 34 ± 2% of its weight by Day 7 in bile ($p < 0.001$). By Day 35, degradation plateaued, suggesting complete CollMA loss and PCL persistence.

2.5. The CBD-Like Construct Modulates Immune Responses, Promoting Tissue Repair while Minimizing Inflammation

Undesirable immune responses can interfere with the proper functioning of engineered constructs in vivo, and minimizing them is therefore a key factor in their success. To evaluate immune responses to our CBD-like construct, we used an ex vivo human whole blood assay. Peripheral blood from three healthy donors was exposed to the acellular construct for 4 and 24 h, and levels of cytokines, chemokines, and growth factors were measured using a Luminex multiplex assay, comparing them to those in blood treated with lipopolysaccharide (LPS), a classical inflammatory stimulus, and untreated (control) blood.

The CBD-like construct did not significantly alter the levels of most immune markers, indicating minimal effect on immune

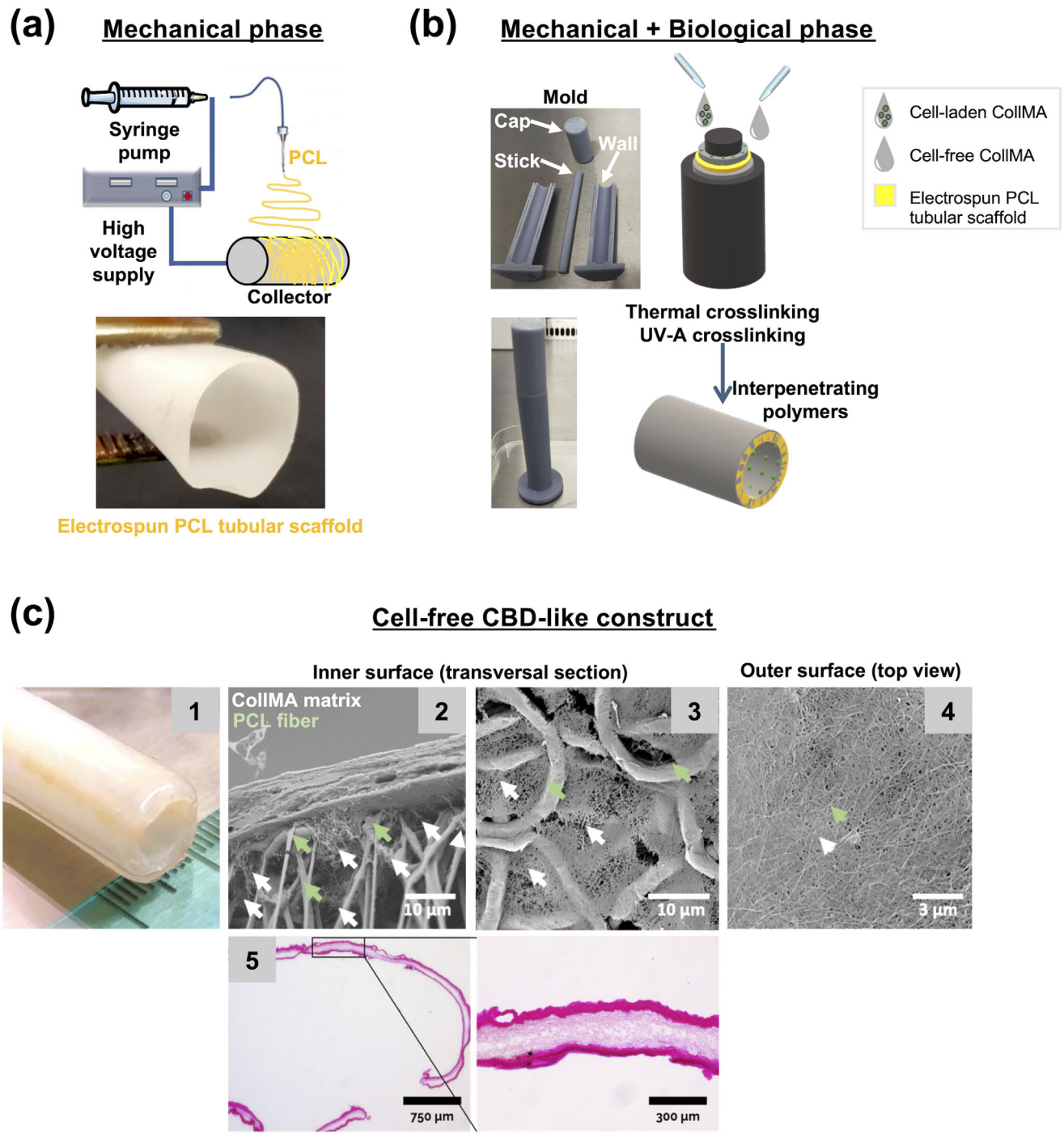

Figure 1. Biofabrication strategy for the generation of a CBD-like construct. Our CBD-like construct is a multiphasic scaffold composed of both a mechanical and a biological phase. The mechanical phase consists of a PCL-based tubular scaffold, which is generated by electrospinning (a). This scaffold (depicted with forming fibers in yellow) is inserted into a 3D-printed tubular mold made up of four components: two half hollow cylinders with flat bases (walls) that combine to form an open-top hollow cylinder via a sliding closure system; a cylindrical stick that fits inside the open-top cylinder; and a removable cap with a pocket to hold the stick, keeping it aligned at the center of the hollow cylinder while sealing the top end (b, left upper panels). Next, drops of a cell-CollMA mixture (depicted as a dotted drop) are poured into the mold between the PCL scaffold and the mold's central stick to form the biological phase of the CBD-like construct (depicted as green dots on a gray background; b, upper right panels). Additionally, drops of a cell-free CollMA solution (depicted as an empty drop) are poured between the PCL scaffold and the mold's walls (depicted in gray; b, upper right panels). After thermal and UV-A-induced polymer crosslinking, a multiphasic construct with three interpenetrating phases measuring 60 × 5 × 2 mm (length × inner diameter × wall thickness) is obtained (b, lower right panels). Panel (c) illustrates: 1) the macroscopic appearance of a cell-free CBD-like construct shortly after biofabrication; 2–4) the interpenetration of PCL and CollMA, as observed by SEM; and 5) the absence of delamination, as confirmed by H&E staining.

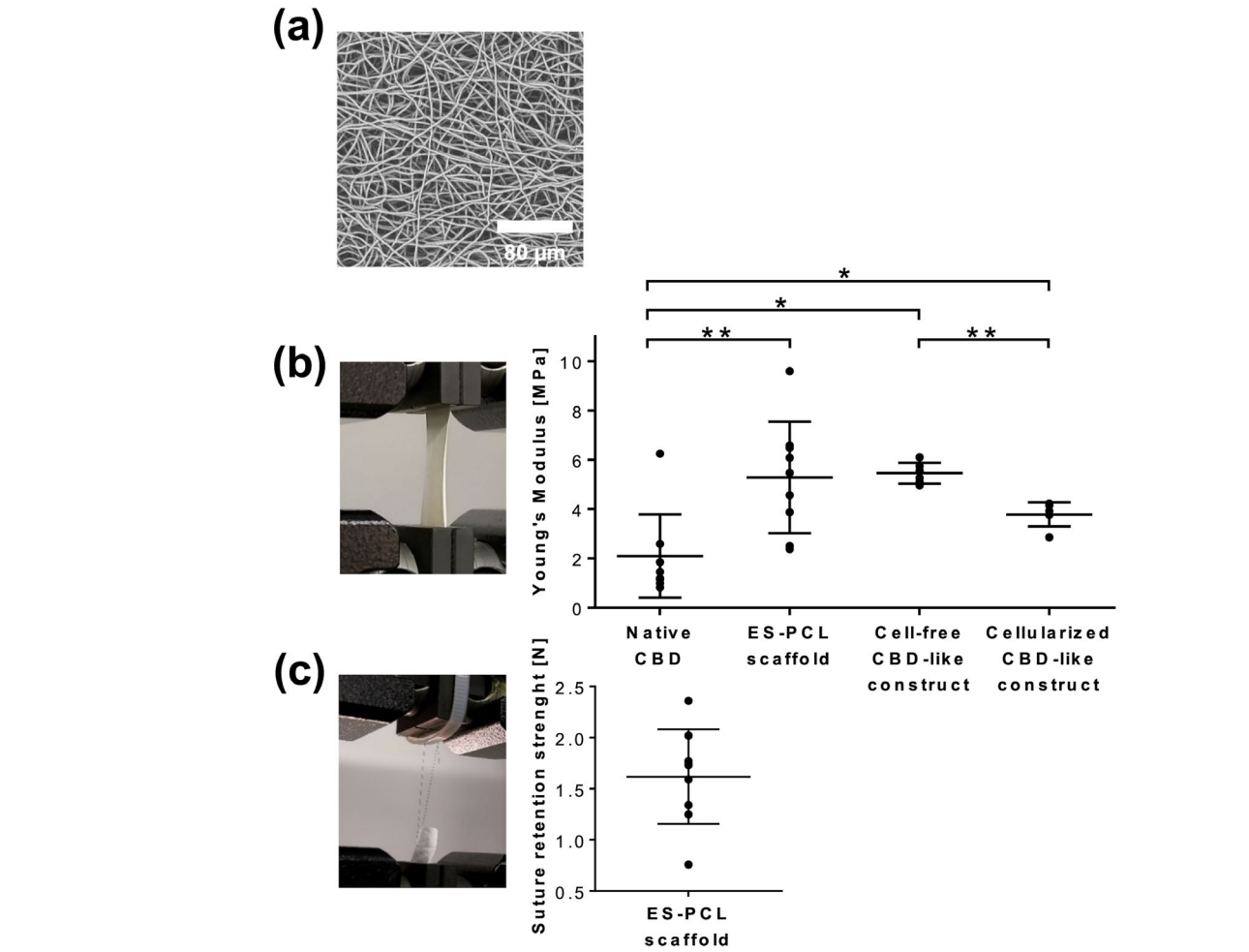

	Leakage rate (%)		Leakage rate (%)
ES-PCL scaffold #1	5	Cell-free CBD-like construct #1	0
ES-PCL scaffold #2	6	Cell-free CBD-like construct #2	0
ES-PCL scaffold #3	7	Cell-free CBD-like construct #3	0
Mean ± SD	6 ± 1	Mean ± SD	0

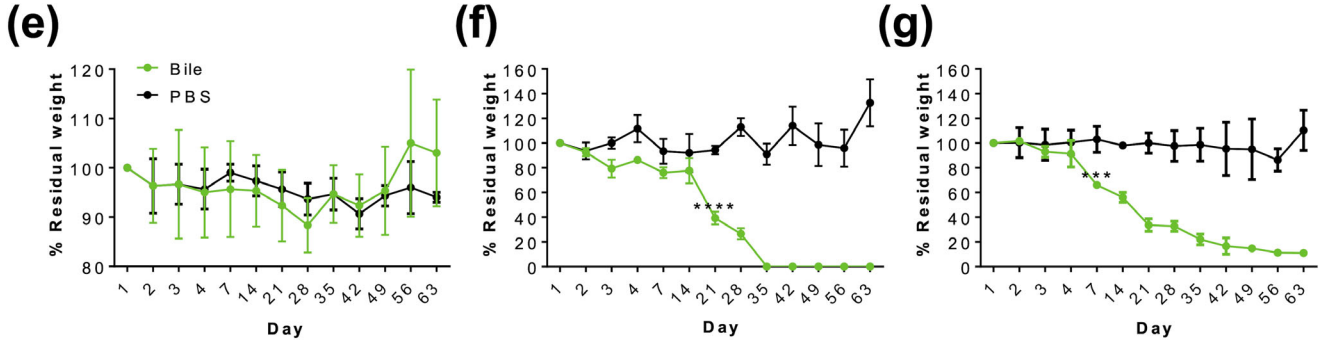

Figure 2. Structure, mechanical properties, and degradation behavior of the CBD-like construct's PCL-based mechanical phase. a) Representative SEM image of the ES-PCL scaffold showing PCL fibers. b) Representative image of an ES-PCL scaffold undergoing a uniaxial test (left), and a graph of Young's Modulus (*E*) values expressed in MPa for native porcine CBD ($N = 9$), ES-PCL scaffold ($n = 9$), cell-free CBD-like construct ($n = 6$), or 14-day cellularized CBD-like construct ($n = 6$) (right). Data are presented as mean ± SD, with each dot representing a technical or biological replicate. The ES-PCL scaffolds

activation. In contrast, as expected, LPS treatment induced significant increases in many markers, particularly at 24 h (**Figure 3a**).

Notably, the CBD-like construct induced a slight but significant increase in IL-7, with levels rising by an average of 2.4-fold ($p < 0.05$) at 24 h (Figure 3b). However, this increase was much smaller than the 450.4-fold rise observed in response to LPS treatment ($p < 0.0001$). Both the CBD-like construct and LPS similarly caused significant rises in MCP-1 (CCL2) levels after 24 h, with average increases of 12.4-fold ($p < 0.05$) and 8.5-fold ($p < 0.05$), respectively (Figure 3c). Additionally, the CBD-like construct prevented the natural decline of RANTES (CCL5). While RANTES levels significantly decreased in the control blood samples from 4 to 24 h ($p < 0.01$), exposure to both the construct and LPS prevented this decline (Figure 3d). Consequently, RANTES levels in the blood exposed to both the construct and LPS were significantly higher than in control samples at 24 h, with average increases of 3.39-fold and 3.96-fold, respectively ($p < 0.001$).

Interestingly, exposure to the CBD-like construct resulted in a significant increase in EGF levels compared to both control and LPS-treated blood at both time points. EGF levels in the construct-exposed blood increased by an average of 104.46-fold at 4 h ($p < 0.0001$) and 272.92-fold at 24 h ($p < 0.0001$), compared to control blood (Figure 3e). The difference between these two time points was also significant ($p < 0.001$), suggesting a time-dependent and sustained release of EGF induced by the construct. In contrast, LPS treatment did not lead to a significant increase in EGF levels at 4 h, though a slight increase was observed at 24 h ($p < 0.05$), averaging 3.84-fold. This suggests that the CBD-like construct promotes a more sustained release of EGF, whereas LPS induces a weaker response.

These results demonstrate that the CBD-like construct can selectively modulate immune responses by inducing slight elevations in IL-7 and MCP-1, preventing the decline of RANTES, and promoting sustained EGF release without triggering the widespread inflammatory activation seen with LPS. The increase in IL-7 and MCP-1 levels, along with the maintenance of RANTES at 24 h, may suggest potential for modulating immune cell recruitment[43,44] as well as T cell survival and activation,[45] both crucial for tissue repair. Moreover, given EGF's ability to accelerate wound healing by stimulating epithelial regeneration,[46] its presence could facilitate the construct's integration with surrounding tissue, promoting more efficient and rapid tissue repair.

2.6. Three Million Cells/ML And 6 MgML^{-1} CollMA are Optimal Conditions for Sustained Biliary Epithelial Cell Growth

An engineered tissue should ideally function and integrate with the host tissue, outcomes that can be better achieved when a cellular component is included. To develop a biologically relevant CBD-like construct, we first optimized cell embedding conditions using the HuCCT1 cholangiocellular carcinoma cell line. To improve cost-efficiency, we used a small-scale construct consisting of a cell-laden CollMA disk, representing the innermost (biological) layer of our bioengineered CBD-like construct (Figure S1, Supporting Information, upper panels). We tested three concentrations of CollMA (4, 6, or 8 mgmL^{-1}), each embedded with 3 million cells/mL, and assessed cell viability over seven days using alamarBlue (Figure S2a, Supporting Information) and LIVE/DEAD assay (Figure S2b, Supporting Information). The 8 mgmL^{-1} CollMA concentration resulted in low viability, likely due to excessive scaffold rigidity, and was therefore excluded. The 4 and 6 mgmL^{-1} concentrations both supported viability, but by Day 7, the 4 mgmL^{-1} CollMA condition showed significantly lower viability ($p < 0.01$). In addition, the 6 mgmL^{-1} CollMA concentration enabled the fabrication of a more stable and manageable tubular structure (data not shown), making it the preferred option for further experiments.

We then optimized cell density by embedding HuCCT1 cells in 6 mgmL^{-1} CollMA at densities of 1, 3, or 5 million cells/mL. High cell viability was maintained with both 3 and 5 million cells/mL, but declined significantly within five days with 1 million cells/mL (Figure S2c,d, Supporting Information). Between the two higher densities, we chose 3 million cells/mL, as it meets the clinical goal of minimizing cell numbers while maintaining efficacy. Thus, we identified 3 million cells/mL and 6 mgmL^{-1} CollMA as the optimal conditions for sustained biliary epithelial cell growth.

2.7. Biliary Epithelial Cells in CollMA Maintain High and Stable Viability for at Least 14 Days with Minimal Proliferation

After identifying the optimal CollMA concentration and cell density, we sought to define the ideal time window for cell viability, reorganization, and function in the scaffold—critical for determining transplant readiness. Cell viability was assessed over 14 days using alamarBlue and LIVE/DEAD assays, showing

show a higher Young's Modulus than native CBDs (**, $p < 0.01$, Mann-Whitney test). Adding CollMA to ES-PCL does not affect Young's Modulus. The cellularized CBD-like constructs show a significant reduction in Young's modulus compared to the cell-free construct (**, $p < 0.01$), approaching native bile duct stiffness, though still distinct (*, $p < 0.05$). c) Representative image of an ES-PCL scaffold undergoing a suture retention strength test (left), and a graph of suture retention strength values expressed in N (right). Data are presented as mean ± SD, with each dot representing a technical replicate ($n = 9$). d, left) Picture of the circuit used for the perfusion of porcine bile within the cell-free CBD-like construct. The peristaltic pump delivers bile into the construct using a bile-filled syringe and silicone tubing. Leaked bile is collected in a Petri dish, while circulated bile is collected in a conical tube. d, right) Rate of bile leakage, expressed as a percentage, from the ES-PCL scaffold or the cell-free CBD-like construct. e–g) Graphs of residual weight expressed as a percentage of control (Day 1) for the ES-PCL scaffold (e), the cell-free CollMA tubular structure (f), or the cell-free CBD-like construct containing both the ES-PCL and the CollMA scaffold (g), after incubation in porcine bile (green line and dots) or PBS (black line and dots), over the course of 63 days. Data are presented as mean ± SD, with each dot representing the average of technical replicates from one representative experiment. A two-way ANOVA was used to calculate statistical significance. No significant weight variations were observed for the ES-PCL scaffold (e) in bile or PBS. Conversely, the weight of the cell-free CollMA tubular structure (f) significantly reduced after exposure to bile, starting from Day 14 (Day 21 versus Day 1: ****, $p < 0.0001$), with complete degradation by Day 35. Similarly, the weight of the cell-free CBD-like construct, which contains both the ES-PCL and CollMA scaffold (g), significantly reduced starting from Day 7 (Day 7 versus Day 1: ***, $p < 0.001$). This is attributable to CollMA scaffold degradation. The weight then stabilized at Day 35, due to the permanence of the ES-PCL scaffold.

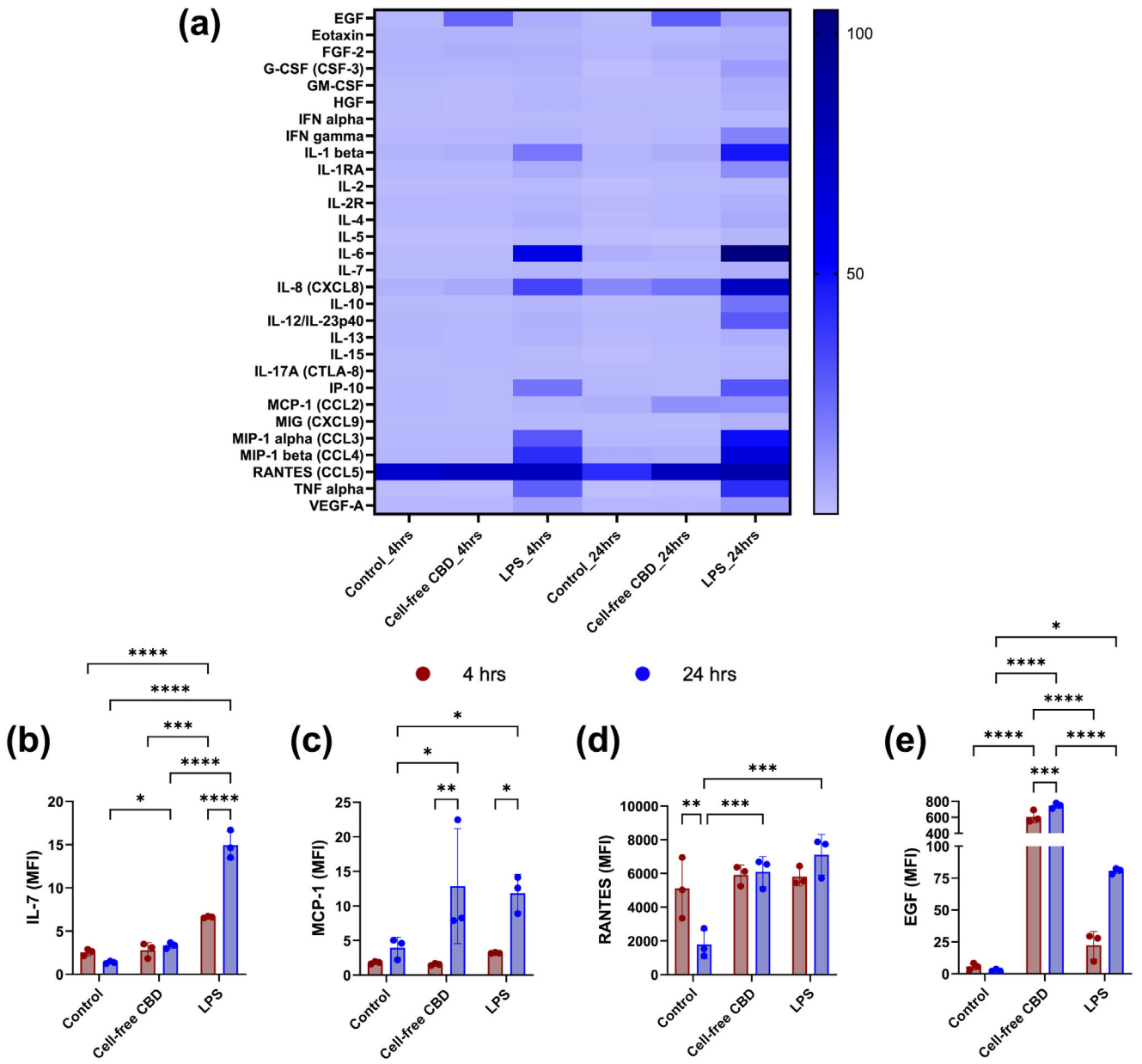

Figure 3. Ex vivo human whole blood assay to evaluate immune system responses to the cell-free CBD-like construct. a) The heatmap shows the expression levels of cytokines, chemokines, and growth factors in blood exposed to the cell-free CBD-like construct or 1 μgmL^{-1} LPS for 4 or 24 h, compared to untreated (control) blood. The square root-transformed MFI values are presented as the mean of measurements from three different blood donors, with the color scale ranging from light violet (smallest) to bright blue (baseline) to dark blue (largest). Graphs of MFI values for IL-7 (b), MCP-1 (c), RANTES (d), and EGF (e) in the same samples as in (a). Data are presented as mean ± SD, with each dot representing MFI values from a blood donor. For MCP-1, the values were square root-transformed, whereas IL-7, RANTES, and EGF are presented as untransformed values. Statistical significance was assessed using ANOVA for multiple comparisons, followed by Tukey's post-hoc test. (*, $p < 0.05$; **, $p < 0.01$; ***, $p < 0.001$; ****, $p < 0.0001$).

consistently high and increasing viability (Figure S3a, Supporting Information), further confirmed by propidium iodide (PI) staining (Figure S3b,c, Supporting Information). To evaluate proliferation, we performed an EdU-based assay by incubating cell-laden disks with EdU on Day 0, 6, or 13, and quantifying labeled cells the following day. Proliferation was minimal and mostly limited to Day 1 (Figure S3d,e, Supporting Information), decreasing significantly over time and nearly absent by Day 14 (Figure S3d,e, Supporting Information), in line with the low turnover of biliary epithelial cells in vivo.[47] Apoptosis remained consistently low, averaging less than 1% at all time points (Figure S3f,g, Supporting Information).

Overall, these results indicate that biliary epithelial cells in CollMA remain viable for at least 14 days with minimal proliferation—an ideal characteristic for successful transplantation. This stable, low-proliferative epithelial layer helps reduce

the risks of polarity loss, overgrowth, and dedifferentiation, thereby minimizing the potential for stenosis and preserving ductal function.

2.8. Biliary Epithelial Cells in CollMA Reorganize into a Biliary-Like Epithelium by Day 14

To assess whether biliary epithelial cells could effectively reorganize in CollMA, we conducted histological and immunoistochemical analyses on cell-laden CollMA disks at Days 7 and 14. The native CBD consists of three layers: the epithelium, subepithelial stroma, and peribiliary connective tissue. The CBD epithelium contains numerous depressions, or sacculi of Beale, where mucous glands in the peribiliary tissue drain (**Figure** 4a). In CollMA disks, cells reorganized to form an epithelial layer with similar depressions (Figure 4b), which was more developed at Day 14 than at Day 7 (Figure 4b). Immunofluorescence confirmed expression of biliary epithelial markers like cytokeratin 7 (CK7), gamma-glutamyl transferase (GGT), secretin receptor (SCTR), anion exchange protein 2 (AE2), aquaporin 1 (AQP-1), and multidrug resistance-associated protein 2 (MRP2) (Figure 4c). Interestingly, cells also expressed bile salt export pump (BSEP), typically found in hepatocytes at the canalicular membrane, likely due to their intrahepatic nature (Figure 4c).[48] Additionally, E-cadherin (ECAD), a key mediator of cell–cell adhesion, which is crucial for tissue morphogenesis and polarity,[49] was expressed (Figure 4c). The levels of five of these markers—CK7, GGT, SCTR, BSEP, and ECAD—were higher at Day 14 compared to Day 7 (Figure 4d).

Biliary epithelial cells secrete mucins to protect against stress-induced damage.[50] Since mucin production indicates functional differentiation, we also examined the expression of MUC5B and MUC5AC, finding increased levels at Day 14 (Figure 4e).

In conclusion, CollMA supports the reorganization of biliary epithelial cells and promotes their functional maturation.

2.9. Biliary Epithelial Cells in CollMA Possess Transport Activity

In addition to assessing cell reorganization and maturation, we evaluated cell function in CollMA by testing their ability to transport fluorescent molecules. First, we used cholyl-L-lysyl-fluorescein (CLF), a fluorescent bile acid analog taken up by organic anion transporter proteins (OATPs) and secreted via BSEP and MRP2.[51] Prior to testing, we confirmed expression of OATP1 (**Figure** 5a), along with BSEP and MRP2 (Figure 4c). Fluorescein isothiocyanate (FITC), which is taken up but not exported, served as a control (Figure 5b).[52] Cells in CollMA successfully transported CLF, though export significantly decreased by Day 14 (Figure 5c,d).

We also assessed the export of the 3,3′-diethyloxacarbocyanine iodide [$DiOC_2(3)$] fluorescent dye, a P-glycoprotein (P-gp/MDR1) substrate. Live imaging showed consistent export from Day 7 to 14 (Figure S4a, Supporting Information), with reduced export upon treatment with vinblastine (VB), a competitive P-gp substrate, confirming specificity (Figure S4b, Supporting Information).

2.10. Increased Levels of Proteins with Sorting and Trafficking Roles During Biliary Epithelial Cell Reorganization in CollMA

So far, we have shown that CollMA supports the formation of a functional biliary-like epithelium. To explore the molecular mechanisms behind this, we performed mass spectrometry-based proteomic analysis of cell lysates from Day 7 and 14 CollMA disks. Among 2003 proteins, 39 proteins were differentially expressed (**Figure** 6a), with Mx1 showing the greatest increase at Day 14 (Figure 6b). Although initially identified as an antiviral protein regulated by type I interferons (IFNs),[53] Mx1 is now known to support intracellular membrane trafficking[54] by associating with endoplasmic reticulum (ER) and endosomal membranes, and by interacting with microtubule-associated proteins, thereby facilitating the transport of apical vesicles along microtubules.[55]

In addition to Mx1, two other IFN-regulated proteins, IFI16[56] and ISG15,[56] were also upregulated at Day 14 (Figure 6b). Like Mx1, they have roles beyond antiviral defense: IFI16 supports microtubule formation,[57] while ISG15 is involved in protein sorting and transport.[58] Complement protein C3, known for its immune functions and role in endosome remodeling[59,60] was also more abundant at Day 14 (Figure 6b). Furthermore, proteins linked to endo-lysosomal trafficking—SBF1, an inactive myotubularin family member,[61] and DHRS9, a moonlighting protein (NCBI_Gene:10 170)—were elevated at Day 14 (Figure 6b).

Biliary epithelial cells are physiologically polarized, with distinct apical and basolateral membranes. We hypothesize that the increased expression of Mx1, IFI16, ISG15, C3, SBF1, and DHRS9 at Day 14 reflects enhanced signaling related to protein sorting, targeting, and distribution— processes that may support ongoing cell polarization and tissue reorganization.

2.11. Increased Levels of ECM-Related Proteins During Biliary Epithelial Cell Reorganization in CollMA

Tissue homeostasis relies on tightly regulated ECM deposition, modification, degradation, and organization.[62] Our proteomic analysis further showed that Day 14 samples had higher levels of proteins involved in these processes, such as AGRN, COL1A2, ITGA2, FN1, TINAGL1, and ITGA5, compared to Day 7 (Figure 6c,d; Table S1, Supporting Information). Day 14 samples also showed higher levels of less common ECM-related proteins, including LCN2, TYMP, SERPINA1, and AGR2 (Figure 6c; Table S1, Supporting Information).

We speculate that as biliary epithelial cells reorganize in CollMA, they modulate all four ECM remodeling mechanisms, gradually forming a matrix that supports functional tissue development.

2.12. Increased Levels of Proteins with Roles in Cell Survival and DNA Damage Repair During Biliary Epithelial Cell Reorganization in CollMA

Mammalian cells have developed various stress responses to maintain homeostasis, including mechanisms that promote cell survival and DNA repair.[63] We identified four such proteins—

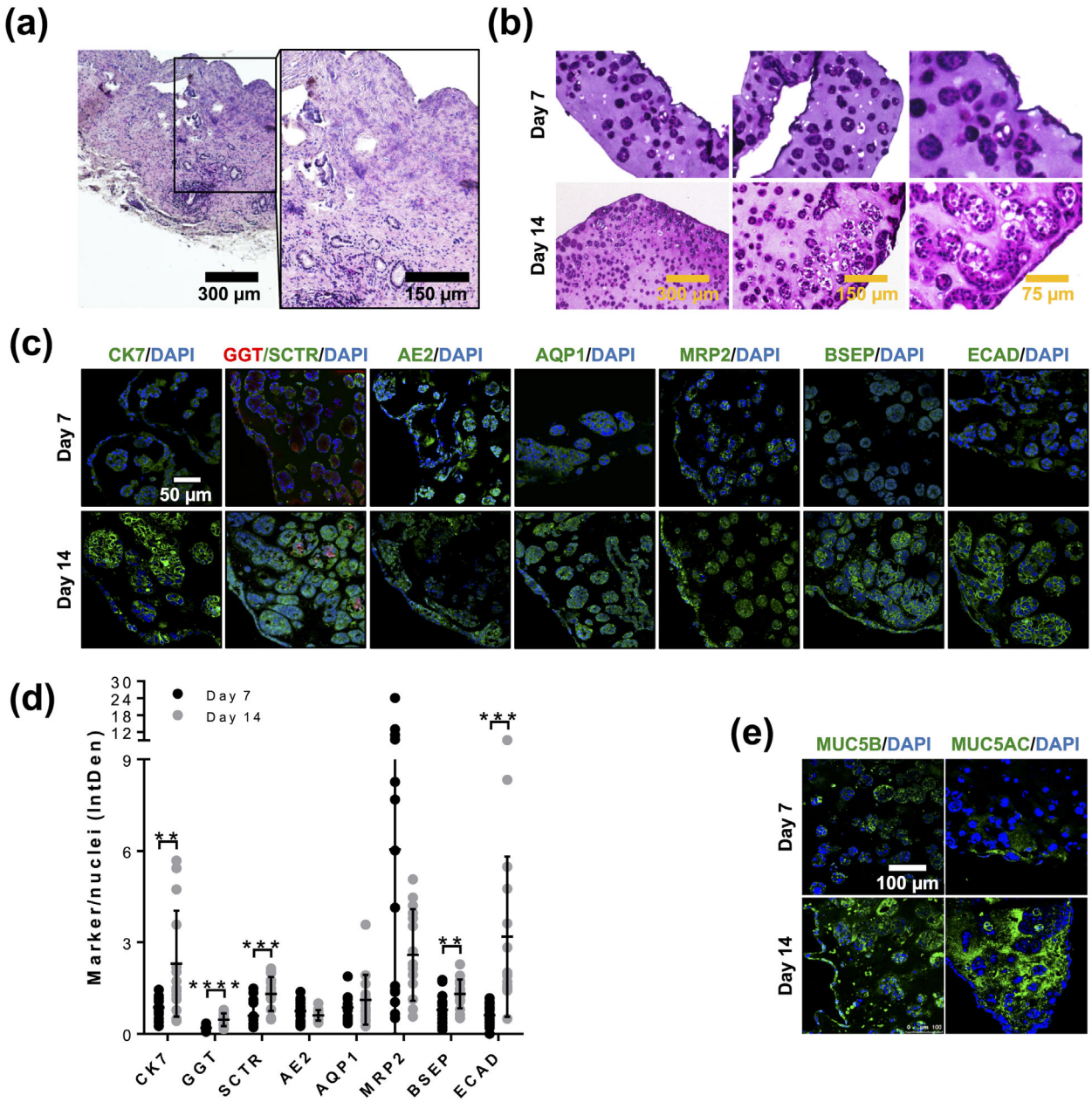

Figure 4. Biliary epithelial cell reorganization and marker expression in CollMA disks. Representative images of H&E-stained paraffin sections of native porcine CBD tissue (a) and cell-laden CollMA disks at Day 7 or 14 (b) ($n = 3$/group). c) Representative confocal images of immunofluorescence staining of sections as in (b) for: CK7 (green), GGT (red), SCTR (green), AE2 (green), AQP1 (green), MRP2 (green), BSEP (green), and ECAD (green) ($n = 3$/group). Nuclei were stained with DAPI (blue). d) Graph showing cell marker expression at Day 7 (black dots) compared to Day 14 (gray dots), expressed as the ratio of the integrated density (IntDen) for each marker over corresponding nuclei. Three independent disks and five fields per disk were analyzed for each group. Data are presented as mean ± SD, with each dot representing marker expression in an individual image field. Statistical significance was assessed by unpaired *t* test (**, $p < 0.01$; ***, $p < 0.001$; ****, $p < 0.0001$). e) Representative confocal images of immunofluorescence staining of sections as in (b), for MUC5B and MUC5AC (green) ($n = 3$/group). Nuclei were stained with DAPI (blue).

ASS1, FBP1, H2AFX, and FTH1—that were significantly elevated on Day 14 compared to Day 7 (Figure S5a, Supporting Information). ASS1, essential for arginine biosynthesis,[64] is strongly expressed in regenerating intestinal epithelium[65] and may contribute to biliary tissue formation. FBP1, important in glucose metabolism, also influences the DNA damage response.[66] H2AFX, a variant of histone H2A, is a key DNA damage response protein,[67] while FTH1 acts as a major antioxidant with ferroxidase activity.[68]

We hypothesize that the expression of these proteins supports biliary epithelial cell reorganization in CollMA by promoting survival and repair mechanisms.

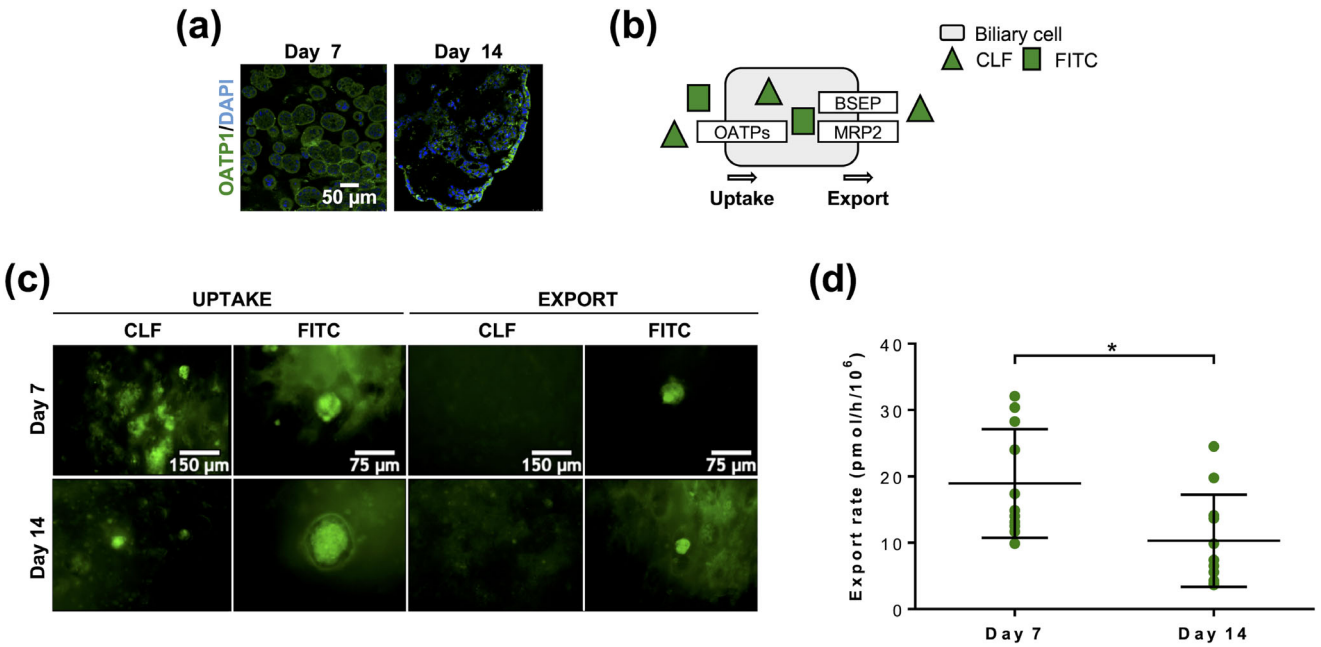

Figure 5. Biliary epithelial cell function in CollMA disks. a) Representative confocal images of immunofluorescence staining of paraffin sections of cell-laden CollMA disks at Day 7 or 14 for OATP1 (green). Nuclei were stained with DAPI (blue). b) Schematic illustration showing the principle of the functional assay based on the use of the fluorescent bile salt derivative CLF. The fluorescein-conjugated CLF (represented by a green triangle) is imported into the biliary epithelial cells by OATP family transporters and is subsequently exported into the medium via BSEP or MRP2 transporters. In contrast, the FITC control (represented by a green rectangle) is imported into the cell by the same family of transporters but cannot be exported into the medium. c) Representative fluorescence live cell imaging to visualize CLF or FITC in cell-laden CollMA disks at Day 7 or 14 during the uptake and export phases ($n = 3$/group). d) Rate of CLF export, as calculated by normalizing the amount of exported fluorescent dye to the number of cells in the construct (in millions) and elapsed time (in hours) for export. Five independent experiments were performed, with a total of eleven disks per group considered. Data are presented as mean ± SD, with each dot representing a disk. The export activity at Day 14 is significantly lower than at Day 7 (*, $p < 0.05$, unpaired t test).

2.13. Decreased Levels of Proteins with Roles in Proliferation, Transcriptional, and Translational Regulatory Networks During Biliary Epithelial Cell Reorganization in CollMA

A total of 19 proteins were significantly decreased at Day 14 compared to Day 7 (Figure 6a, blue dots). These included proteins involved in DNA replication (MCM7, MCM3, DUT, MCM4, DTYMK, PCNA, RBBP7, NASP; **Figure** 7a,b), cell division (CNN3, STMN1; Figure 7a), transcriptional regulation (ABCF1 and PPM1G; Figure 7c), and translational regulation, protein synthesis, and protein homeostasis (RPL35A, CSDE1, DNAJC7, BZW2, and TRIP13; Figure 7c). Levels of UAP1 and MT2A, involved in cell proliferation, also declined. Full details are provided in Table S2 (Supporting Information).

The temporal coordination between proliferation and differentiation is crucial for normal development,[69] and our data suggest that between Day 7 and Day 14, biliary epithelial cells shift from proliferative, transcriptional, and translational programs toward polarization and morphogenesis. This is supported by reduced proliferation (Figure S3d,e, Supporting Information), decreased CLF export (Figure 5c,d), and more advanced tissue organization at Day 14 (Figure 4b–e).

Functional enrichment analysis using FunRich[70] confirmed that proteins upregulated at Day 14 were enriched in Gene Ontology (GO) terms related to transport and ECM, while downregulated proteins were associated with DNA, RNA, and protein metabolism (Figure S5b,c, Supporting Information). Notably, exosomes emerged as a key cellular component linked to increased proteins (Figure S5d, Supporting Information). As exosomes can interact with and remodel the ECM,[71] we speculate that the Day 14 protein signature reflects both enhanced membrane trafficking and exosome-mediated ECM organization.

2.14. Biliary Epithelial Cells Reorganizing in CollMA Downregulate Major Energy-Consuming Pathways Likely to Support ECM Remodeling

To investigate whether putative exosome-guided polarization and ECM remodeling begin early during biliary epithelial cell reorganization in CollMA, and to assess phenotypic changes induced by the 3D collagen matrix, we compared Day 7 CollMA-embedded biliary epithelial cells with their parental cells in 2D culture. Proteomic analysis identified 2151 proteins, with 308 differentially expressed (**Figure** 8a; Table S3, Supporting Information). Of the six previously noted transport-related proteins, only C3 was more abundant in 3D. However, using less stringent criteria (Log2FC ≥ 0.59), 32 proteins linked to vesicle-mediated transport and cellular localization were upregulated (Figure S6a,b, Supporting Information), supporting early activation of vesicular transport during reorganization in CollMA.

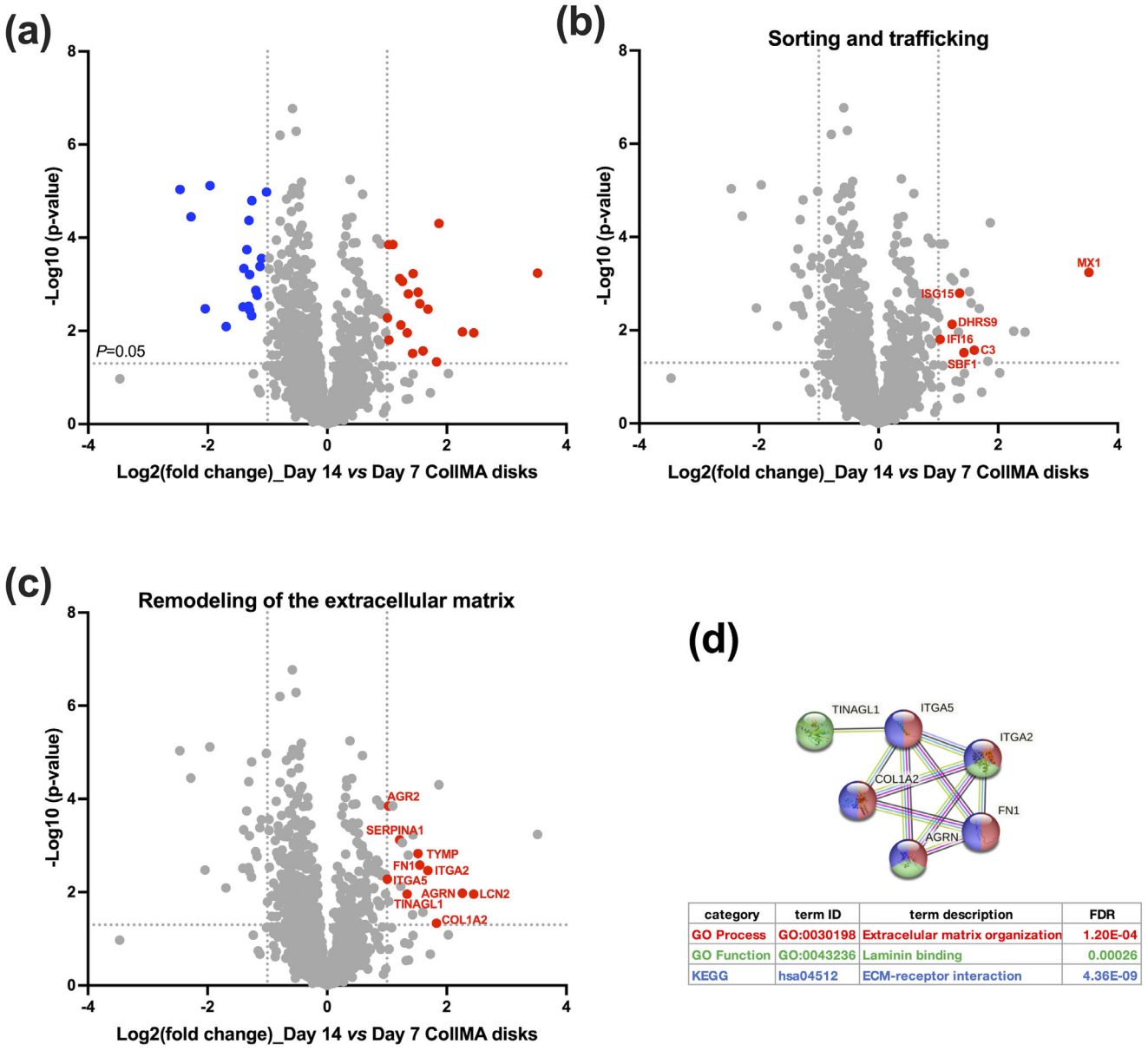

category	term ID	term description	FDR
GO Process	GO:0030198	Extracelular matrix organization	1.20E-04
GO Function	GO:0043236	Laminin binding	0.00026
KEGG	hsa04512	ECM-receptor interaction	4.36E-09

Figure 6. Proteome changes in biliary epithelial cells reorganizing in CollMA disks: increased proteins at Day 14. a–c) Volcano plot representation of differential protein expression between Day 14 and Day 7 cell-laden CollMA disks. The vertical and horizontal dotted lines represent the fold-change cut-off of ± 1 and *p*-value cut-off of 0.05, respectively. Red and blue points indicate proteins with significantly increased or decreased expression, respectively. d) STRING protein–protein interaction networks of selected proteins involved in ECM organization. Node colors correspond to the GO processes, functions, or KEGG annotations, which are listed in the table along with their FDR values.

Compared to their parental cells in 2D culture, Day 7 CollMA-embedded biliary epithelial cells also exhibited increased levels of proteins enriched in GO terms related to ECM organization and collagen hydroxylation—key for stabilizing the collagen triple helix and fibril assembly (Figure 8b; Figure S7a, Supporting Information).[72] Seven of these proteins—AGRN, COL1A2, FN1, LCN2, TYMP, AGR2, and COL1A2—were also elevated at Day 14, suggesting an early and sustained involvement in tissue reorganization. Immunofluorescence confirmed higher expression of collagen-modifying enzymes PLOD2 (procollagen-lysine,2-oxoglutarate 5-dioxygenase 2),[73] P4HA1 (prolyl 4-hydroxylase subunit alpha 1), and P4HA2[74] in Day 7 samples (Figure 8c). Additionally, proteomic analysis confirmed earlier findings of mucin production (Figure 4e), showing increased MUC5AC in CollMA-embedded biliary epithelial cells compared to 2D cultures (Figure 8a).

Cell reorganization is energy-intensive, and metabolic reprogramming—particularly the induction of glycolysis[75]—is often used to meet these demands. Consistent with this, nine glycolytic enzymes, including ENO2, ALDOC, PGK1, HK2, GPI, SLC2A1, LDHA, ALDOA, and TPI1, were more abundant in Day 7 CollMA-embedded biliary epithelial cells compared to

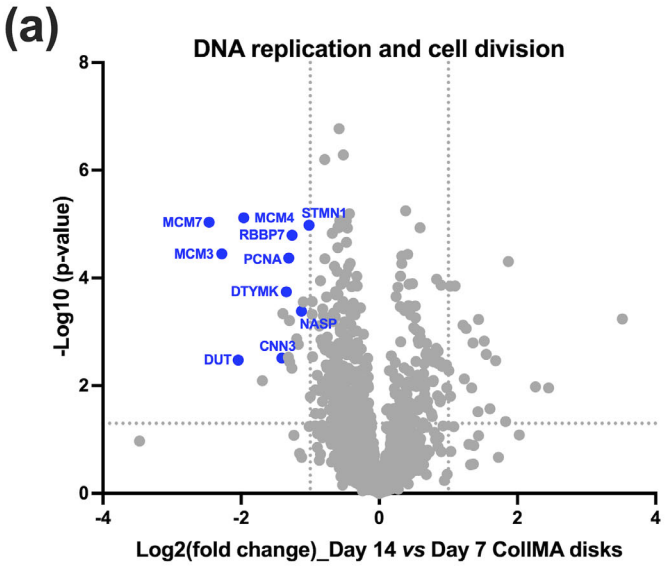

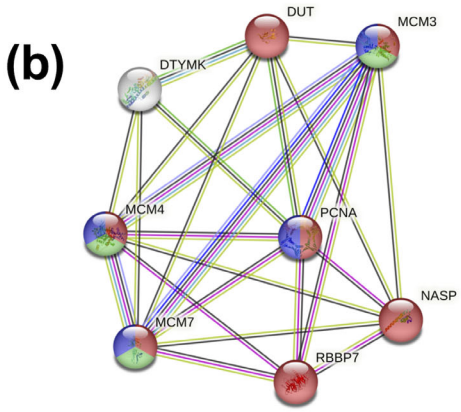

category	term ID	term description	FDR
GO Process	GO:0006260	DNA replication	1.61E-09
GO Function	GO:0003688	DNA replication origin binding	0.00038
KEGG	hsa03030	DNA replication	3.49E-07

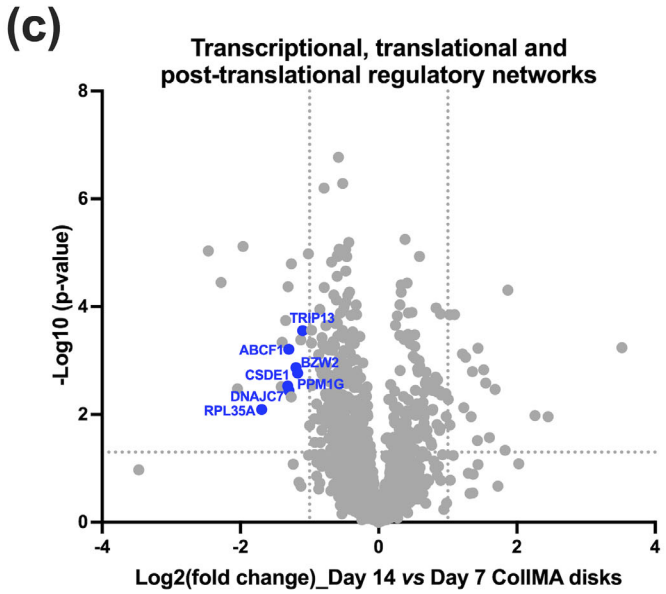

Figure 7. Proteome changes in biliary epithelial cells reorganizing in CollMA disks: decreased proteins at Day 14. a,c) Volcano plot representation of differential protein expression between Day 14 and Day 7 cell-laden CollMA disks. The vertical and horizontal dotted lines represent the fold-change cut-off of ± 1 and *p*-value cut-off of 0.05, respectively. Some proteins that are decreased at Day 14 are labeled. b) STRING protein-protein interaction networks of selected proteins involved in DNA replication. Node colors correspond to the GO processes, functions, or KEGG annotations, which are listed in the table along with their FDR values.

the 2D culture (Figure 8b; Figure S7b, Supporting Informaton). Other glycolysis promoters such as MGEA5,[76] S100 calcium-binding protein A (S100A) family members S100A10, S100A2, S100A6, and S100A11,[77,78] ERO1L,[79] GBE1,[80] IDH2,[81] and the glycosyltransferase GALE[82] were also elevated (Figure 8b; Figure S7b, Supporting Information), supporting a metabolic shift toward aerobic glycolysis during early cell reorganization.

Enhanced glycolysis is a common feature of metabolic reprogramming in response to hypoxia, and eight of the upregulated glycolytic proteins (i.e., GPI, P4HA1, ALDOA, LDHA, HK2, TPI1, SLC2A1, PGK1) are known hypoxia-associated markers. To investigate whether Day 7 CollMA-embedded biliary epithelial cells were experiencing hypoxia, we examined the levels of 51 proteins previously linked to hypoxia in a cancer meta-analysis.[83] Only 11 were significantly elevated, including the eight glycolytic proteins mentioned above, along with NDRG1, MIF, and CHCHD2, suggesting a partial hypoxic response. Interestingly, NDRG1, a stress-responsive protein,[84] was the most highly increased protein in Day 7 CollMA-embedded biliary epithelial cells compared to the 2D culture (Figure 8a). Increased

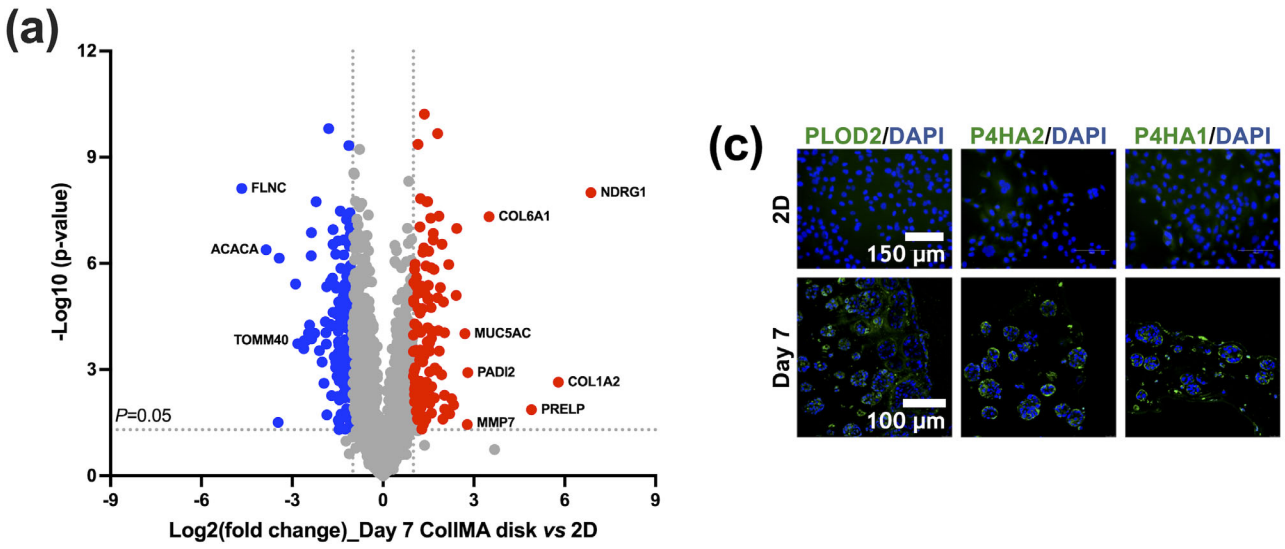

(b)

Process	Proteins
Extracellular matrix and cytoskeleton organization	AGRN, FN1, LCN2, TYMP, AGR2, ITGA6, TSPAN14, CD9, PRELP, ACAN, MMP7, SLFN5, SERPINB1, SERPINB2, SERPINB9, CSTB, PADI2, GSN, AHNAK2, ANXA4, ABRACL, TUBA1A, TUBB8
Collagen biosynthesis	COL1A2, COL6A1, PLOD2, P4HA2, P4HA1
Classical glycolysis	ENO2, ALDOC, PGK1, HK2, GPI, SLC2A1, LDHA, ALDOA, TPI1, MGEA5
Oxidative stress	SOD2, BANF1, CISD1, LGALS1, GLRX, QSOX1, FIS, FAM129B, TXN2, PRDX5, PSAP, CRYZ
Mitochondrial gene expression and mitochondrion organization	TOMM40, CHD4, CHCHD3, KPNA2, ATAD3A, ASNS, IMMT, ACAD9, HCFC1, VDAC3, DAP3, TOMM22, ATAD1, VDAC2, MRPL14, SF3B2, SQSTM1, FASN, PGAM5, MRPL11, YBX1, SLC25A6, NRD1, FXR1, CAV2, NDUFA5, COX6C, PNPT1, MRPS7, SLC25A1, TIMM13, PYCR1, MRPL30, NDUFS1, COA3, MRPL4, STOML2, CYP51A1, VDAC1, MRPS27, MTCH2, GFM1
Translation regulators	RPL13, RPL24, RPL11, RPL22, RPS28, RPL18, RPL34, RPL27A, RPLP2, RPL7A, RPL27, RPL28, THRAP3, CSDE1, FXR2, WIBG, RBM25, ELAVL1, TAF15, HNRNPA2B1, CAPRIN1, HNRNPR, RBMX, FUS, EIF2A, EIF2S2, EIF3C, EIF5B, EIF2B4, EEF1E1
Transcription regulators	FUBP3, LMNB2, BCLAF1, TOP1, XRN2, SMC1A, UPF1, PTRF, ALYREF
Splicing regulators	EFTUD2, HNRNPC, PRPF6, YBX3, SNRNP200, PRPF8, HNRNPU, SRRM1, SNRNP70, RRM1, SF3B1, PRKDC
RNA metabolism	SKIV2L2, DDX46, METTL1, NAT10, MARS
DNA replication	MCM3, MCM2, MCM7, PDS5A, TOP1, SUPT16H, SSRP1, NCL
Cytoskeleton remodeling	FLNC, CKAP5, DSP, FMNL1, SPTBN1, STMN2, SPTAN1, PALLD, TNKS1BP1
Lipid metabolism	ACACA, ACSL4, HMGCS1, RNF213, HACD3, OSBPL3, DHCR7, ACLY, MTHFD1

Figure 8. Proteome changes in biliary epithelial cells reorganizing in CollMA disks for 7 days with respect to their parental cells in 2D culture. a) Volcano plot representation of differential protein expression in CollMA-embedded biliary epithelial cells relative to 2D culture. The vertical and horizontal dotted lines represent the fold-change cut-off of ± 1 and *p*-value cut-off of 0.05, respectively. Red and blue points indicate proteins with significantly increased or decreased expression, respectively. Some of these proteins are labeled. b) List of processes that are altered in Day 7 CollMA-embedded biliary epithelial cells relative to the 2D culture, with associated proteins (red color: enriched; blue color: depleted). Enriched proteins are arranged in descending Log2FC values, while depleted proteins are arranged in ascending Log2FC values. c) Representative confocal images of PLOD2, P4HA2, and P4HA1 immunofluorescence staining (green) in Day 7 cell-laden CollMA disks, compared to 2D culture. Nuclei were stained with DAPI (blue).

NDRG1 expression has been reported in biliary epithelial cell organoids,[85,86] which, like most 3D models, often face an insufficient oxygen supply. NDRG1's role in our system, given its varied effects across tissues,[87] warrants further investigation. Notably, NDRG1 interacts with proteins involved in vesicular trafficking and regulates E-cadherin recycling by acting as an effector for Rab4a, promoting adherens junction stability.[88] Adherens junctions are crucial for establishing tight junctions, which enable apical-basal polarity in epithelial cells.[89] Interestingly, the E-cadherin partner EpCAM, which contributes to functional tight junctions,[90] was also more abundant in Day 7 CollMA-embedded biliary epithelial cells compared to the 2D culture (Table S3, Supporting Information). Additionally, MYH10, involved in tight junction biogenesis,[91] and RAB5A, a master regulator of endosome biogenesis and trafficking,[92] were more abundant in Day 7 CollMA-embedded biliary cells (Table S3,

Supporting Information). These findings suggest that, despite potential hypoxia in CollMA, biliary epithelial cells may still reorganize into functional tissue, potentially benefiting from this environment.

Metabolic reprogramming can also be triggered by oxidative stress.[93] CollMA-embedded biliary epithelial cells likely experience oxidative stress following UV-A exposure for CollMA crosslinking, which may activate antioxidant defenses, as shown by the increased levels of 12 oxidative stress-protective proteins compared to the 2D culture (Figure 8b).

Glycolytic reprogramming is linked to epithelial-mesenchymal transition (EMT). To investigate EMT, we analyzed 200 proteins from the MsigDB v7.0 EMT signature[94] and found only 11 significantly altered in Day 7 CollMA-embedded biliary epithelial cells compared to 2D culture (i.e., COL1A2, ENO2, PLOD2, LGALS1, QSOX1, FN1, IGFBP3, CAPG, EDIL3, MCM7 and SERPINH1). However, none are classical EMT markers,[95] suggesting that EMT is unlikely in our system.

Our proteomic analysis indicated a metabolic shift toward glycolysis during biliary epithelial cell reorganization in CollMA, consistent with previous findings linking glycolysis to ECM remodeling.[75] We also observed a decrease in proteins enriched in GO terms related to mitochondrial gene expression and organization (Figure 8b; Figure S7c, Supporting Information). To investigate if this reflected impairment of the mitochondrial oxidative phosphorylation (OXPHOS) system, we analyzed the expression levels of 149 OXPHOS-related proteins, which we derived from the GO resource GO:0006119. Only eight showed significant differential expression, with CHCHD2 and BID increased, and six proteins (MTCH2, STOML2, NDUFS1, COX6C, NDUFA5, and CDC2) decreased. These results suggest that OXPHOS is not significantly inhibited during biliary epithelial cell reorganization in CollMA.

Not only did the Day 7 CollMA-embedded biliary epithelial cells exhibit a repression of mitochondrial function compared to the 2D culture, but they also showed decreased levels of proteins associated with GO terms related to translational initiation, RNA splicing, and regulation of mRNA metabolic process (Figure 8b; Figure S7d, Supporting Information). Additionally, proteins involved in DNA replication, cytoskeleton remodeling, and lipid metabolism were also reduced (Figure 8b).

These findings suggest that ECM remodeling in CollMA, is accompanied by reprogramming of processes primarily related to mitochondrial function and RNA metabolism, along with measurable alterations in glycolysis, oxidative stress response, cytoskeletal remodeling, lipid metabolism, and DNA replication, though to a lesser extent (Figure S7e, Supporting Information).

2.15. Cell Culture Conditions Optimized using CollMA Disks also Adapt to CollMA Tubular Structures

After optimizing the cell culture conditions for the formation of a functional biliary-like epithelium in CollMA and investigating the underlying molecular mechanisms, we scaled up the culture system to generate a cell-laden CollMA tubular structure, following the approach outlined in Figure S1 (Supporting Information) (lower panels).

For CollMA disks, UV-A cross-linking preceded thermal cross-linking, but for tubular structures, thermal cross-linking was required to first stabilize the hydrogel. This adjustment did not affect cell viability (data not shown) and was considered acceptable.

Using alamarBlue and LIVE/DEAD assays, we first confirmed that the conditions optimized for the disks were also suitable for the tubular structures. Cell viability slightly increased over 14 days (**Figure 9a**), with no dead cells detected at Day 14 by PI staining (Figure 9b). Encouraged by these results, we extended the culture to 28 days, observing sustained viability (Figure S8a,b, Supporting Information), and stable proliferation after a slight decline by Day 7 (Figure S8c, Supporting Information).

H&E showed that by Day 14, cells in the CollMA tubular structures had formed a surface epithelium with small aggregates beneath (Figure 9c), resembling Day 7 disks. Specific biliary epithelial cell markers were confirmed by immunofluorescence staining (Figure 9d). Interestingly, SCTR and BSEP expression were significantly lower in tubes than in disks (Figure 9e). Finally, CLF export at Day 14 was significantly higher ($p < 0.0001$) and more consistent in tubes than disks (Figure 9f,g), matching levels seen in Day 7 disks (Figure 5d).

2.16. The Cellularized CBD-Like Construct Demonstrates High Cell Viability and Function with Cells Arranging Similar to Native Tissue

We previously demonstrated that the cell culture conditions optimized using CollMA disks are also compatible with CollMA tubular structures. Next, we investigated how these cell-laden structures would perform within a complete CBD-like construct that incorporates the PCL-based mechanical phase. We generated this construct as described in Figure 1 and assessed cell viability at Day 14 using the alamarBlue assay (**Figure 10a**), tissue organization via H&E staining (Figure 10b), marker expression and localization through immunofluorescence (Figure 10c,d), and cellular function via the CLF test (Figure 10e) We also compared proteomic profiles of cells in the CBD-like construct with those in the disks (Figure S9a, Supporting Information).

By Day 14, cell metabolic activity had significantly increased compared to Day 0 ($p < 0.0001$; Figure 10a). A surface epithelium and small aggregates resembling native tissue had formed (Figure 10b), including within the PCL-based mechanical phase, indicating cell infiltration. Immunofluorescence confirmed expression of previously analyzed markers and revealed additional ones such as the apical sodium-dependent bile acid transporter (ASBT), cytokeratin 19 (CK19), and somatostatin receptor 2 (SSTR2) (Figure 10c). However, direct comparison of marker expression between the cell-laden CollMA tubular structure and the complete CBD-like construct was not feasible due to differences in embedding methods. Specifically, to preserve the PCL structure, samples were embedded in optimal cutting temperature (OCT) compound rather than paraffin.

We further characterized the tubular scaffolds by staining for zonula occludens-1 (ZO-1) and F-actin (phalloidin), both key indicators of epithelial polarization. ZO-1 staining indicated the formation of an intact epithelial barrier, while F-actin staining highlighted the establishment of apico-basal epithelial polarity (Figure 10d).[96,97] F-actin was observed not

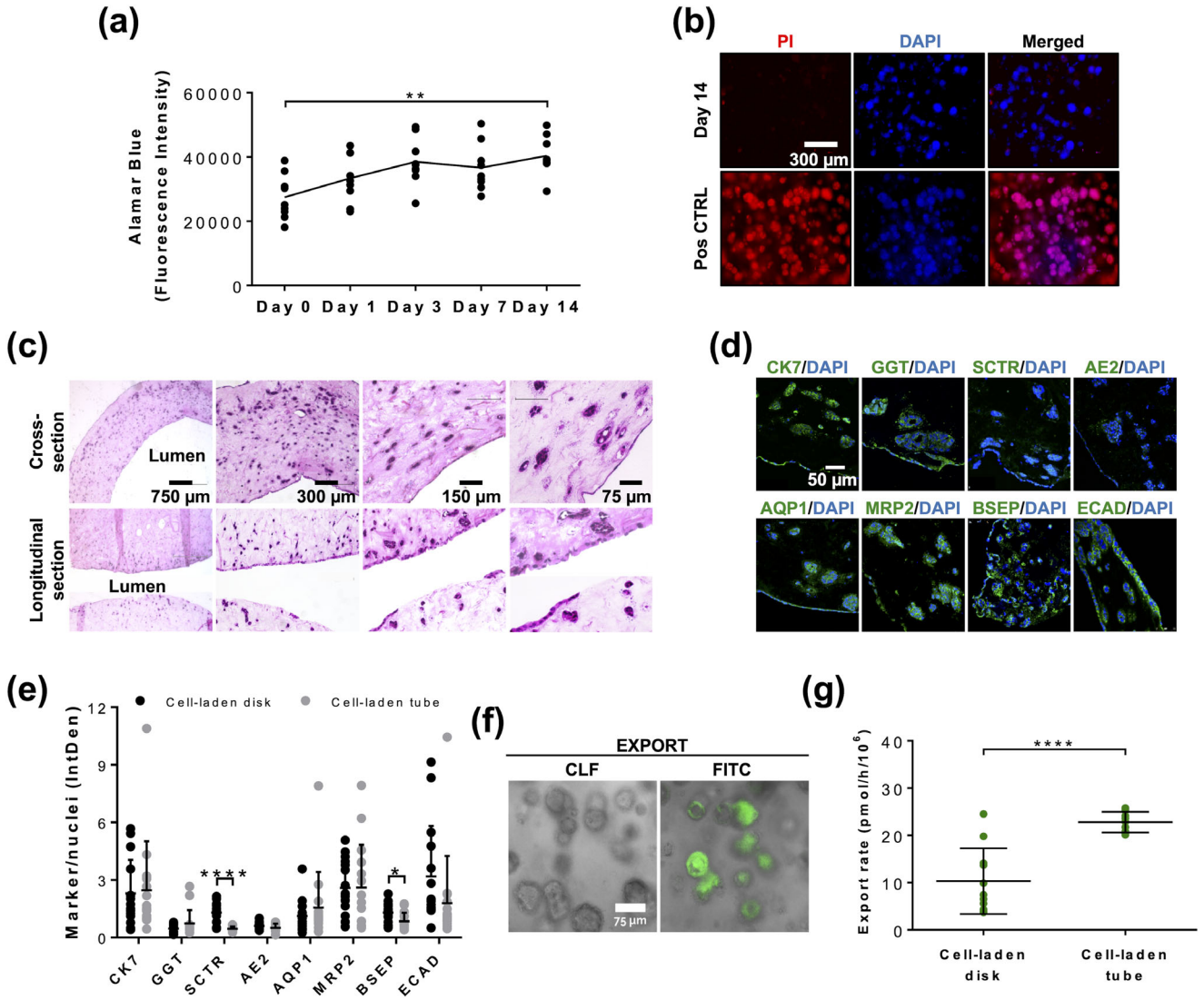

Figure 9. Biliary epithelial cell reorganization and function in CollMA tubular structures. a) Graph of alamarBlue fluorescence intensity in CollMA tubular structures (3 million cells/mL cells in 6 mgmL^{-1} CollMA) over the course of 14 days. Four tubes per time point were generated. Each tube was divided into multiple slices, and a total of 11 slices per time point were subjected to alamar Blue assay. Each dot represents the fluorescence intensity of a tube slice. A mean line is shown. There is a significant increase at Day 14 compared to Day 0 (**, $p < 0.01$, paired t test). b) Representative fluorescence live cell imaging of PI staining (red) in tubes at Day 14, showing dead cells (PI positive) and nuclei (DAPI, blue) ($n = 3$). A positive control of cell death (Pos CTRL) was obtained by exposing cells to 70% ethanol. c) Representative images of H&E-stained paraffin-embedded cross and longitudinal sections of CollMA tubular structures at Day 14 ($n = 3$). The longitudinal sections at the highest magnifications are composites of two images, highlighting the two sides of the luminal epithelium. d) Representative confocal images of immunofluorescence staining of sections of cell-laden CollMA tubular structures at Day 14 for CK7, GGT, SCTR, AE2, AQP1, MRP2, BSEP, and ECAD (green) ($n = 3$). Nuclei were stained with DAPI (blue). e) Graph of cell marker expression in cell-laden CollMA tubular structures (gray dots) compared to cell-laden CollMA disks (black dots), expressed as the ratio of IntDen for each marker over corresponding nuclei. For each group, three independent samples and five fields per sample were considered. Data are presented as mean ± SD, with each dot representing marker expression in an individual image field. Statistical significance was assessed by the Mann-Whitney test (*, $p < 0.05$; ****, $p < 0.0001$). f) Representative merged fluorescence and phase contrast live cell imaging of CLF or FITC in cell-laden CollMA tubular structures at Day 14 during the export phase. g) Rate of CLF export as calculated by normalizing the amount of exported fluorescent dye against the number of cells in the construct (in millions) and elapsed time (in hours) for export. Data are presented as mean ± SD, with each dot representing a technical replicate (eleven per group) from at least three independent experiments. CLF export rate is significantly higher in tubes (****, $p < 0.0001$, unpaired t test).

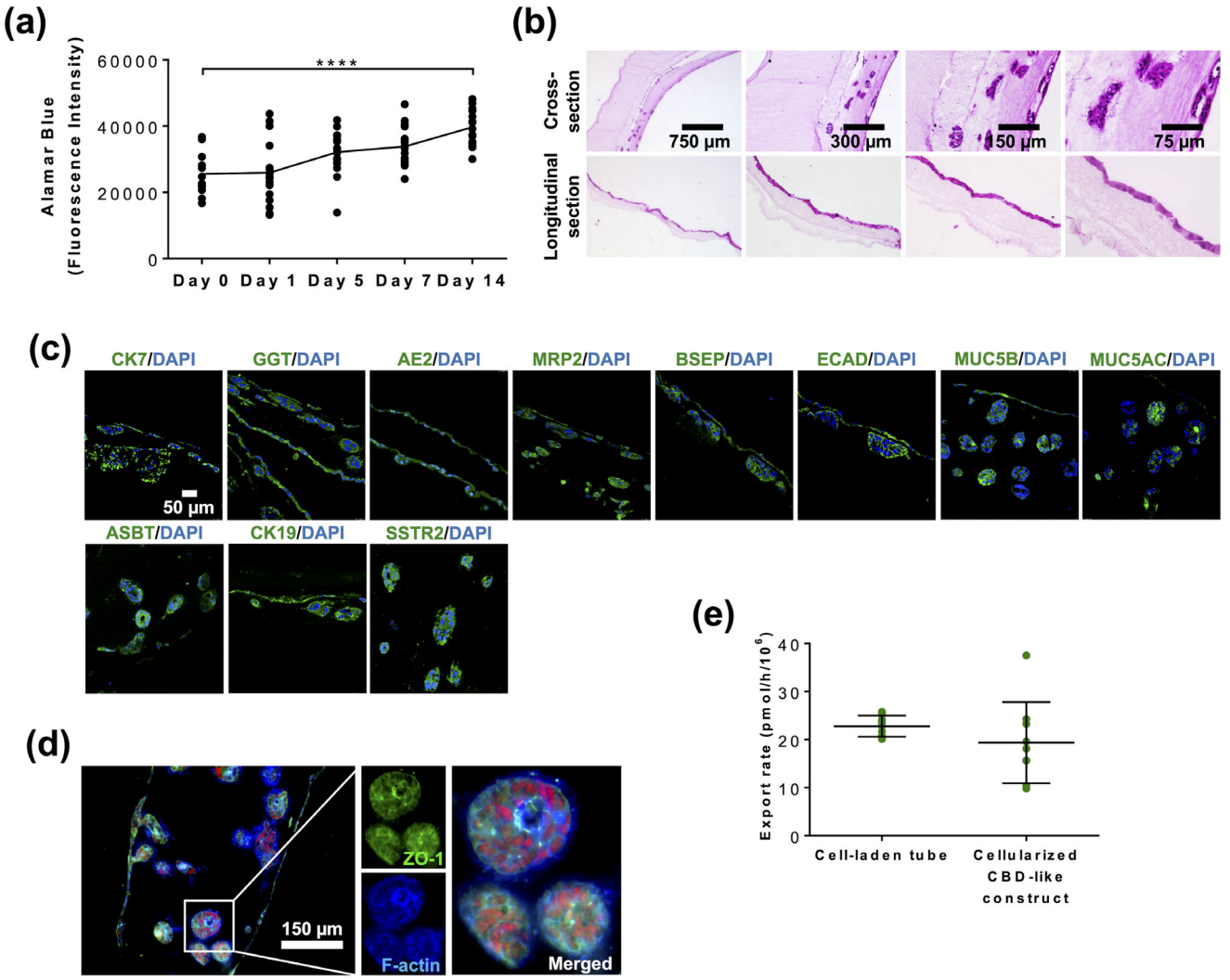

Figure 10. Biliary epithelial cell reorganization, marker expression, and function in the CBD-like construct. a) Graph of alamarBlue fluorescence intensity in the cellularized CBD-like construct (3 million cells/mL cells in 6 mgmL^{-1} CollMA) over the course of 14 days. Four tubes per time point were generated. Each tube was divided into multiple slices, and a total of 17 slices per time point were subjected to alamarBlue assay. Each dot represents the fluorescence intensity of a tube slice. A mean line is shown. There is a significant increase at Day 14 compared to Day 0 (****, $p < 0.0001$, paired t test). b) Representative images of H&E-stained OCT compound-embedded cross and longitudinal sections of the cellularized CBD-like construct at Day 14 ($n = 3$). c) Representative confocal images of immunofluorescence staining of sections as in (b) for CK7, GGT, AE2, MRP2, BSEP, ECAD, MUC5B, MUC5AC, ASBT, CK19, and SSTR2 (green). Nuclei were stained with DAPI (blue). d) Representative confocal images of immunofluorescence staining of sections as in (b) for ZO-1 (green) and F-actin (blue). Nuclei were stained with PI (red). Insets show expression of F-actin in the lumen of the biliary epithelial cell aggregates. e) Rate of CLF export in cell-laden CollMA tubular structure compared to the CBD-like construct at Day 14, as calculated by normalizing the amount of exported fluorescent dye against the number of cells in the construct (in millions) and elapsed time (in hours) for export. Data are presented as mean ± SD, with each dot representing a technical replicate (11 slices of the cell-laden CollMA tubular structure and nine slices of the CBD-like construct) from at least three independent experiments. No significant differences were observed (unpaired t test).

only at the apical surface of the biliary epithelial cells forming the surface epithelium but also within the lumen of the cell aggregates growing beneath, suggesting potential lumen specification.[98]

We then conducted a proteomic analysis to compare cells in the CBD-like construct with those in the disk. A total of 2766 proteins were detected and quantified. Compared to cells in CollMA disks, those in the CBD-like construct showed higher levels of FLNC, a filamin isoform that serves as an F-actin crosslinking protein and is crucial for maintaining structural integrity (Figure S9b, Supporting Information).[74] Additionally, proteins involved in ECM organization and collagen binding—such as POSTN, LUM, VTN, COMP, and TNXB—were more abundant in cells of the CBD-like construct (Figure S9b,c, Supporting Information).

Finally, we compared cell function between the disks and tubes and found similar CLF export rates (Figure 10e).

Overall, the cellularized CBD-like construct supported viability and function, expressed key biliary epithelial cell markers, and showed enhanced apico-basal polarization and ECM remodeling, likely due to its tubular geometry.

2.17. The CBD-Like Construct Cellularized with Cholangiocyte Stem Cells Demonstrates High Cell Viability, Transport Activity, and Bile Modification Properties

Our initial efforts in biliary duct tissue engineering were conducted using HuCCT1 cells. To develop a clinically relevant CBD-like construct, we transitioned to commercially available cholangiocyte stem cells derived from healthy CBD.[99] Using previously optimized culture conditions, we generated constructs with high cell viability (**Figure 11a**), organized epithelium (Figure 11b–d), CLF transport activity (Figure 11e), and bile modification potential (Figure 11f). By Day 14, the cells formed a near-native surface epithelium (Figure 11b), although unlike HuCCT1 cells, they did not form small aggregates. Similar to HuCCT1 cells, cholangiocyte stem cells infiltrated the fibrous PCL structure (data not shown). The biliary epithelium generated by the cholangiocyte stem cells expressed all previously analyzed markers and, in addition, also expressed CFTR (Figure 11c), a chloride (Cl^-) and bicarbonate ion (HCO_3^-) channel absent in HuCCT1-derived epithelium.

Proteomic analysis was performed to compare protein expression in CBD-like constructs cellularized with either HuCCT1 cells or cholangiocyte stem cells (Figure S10a, Supporting Information). A total of 2766 proteins were detected and quantified in these samples. The results indicated that even cholangiocyte stem cells may not be an ideal cell source. Both CBD-like constructs expressed markers of adult biliary epithelial cells, hepatocytes, and bipotential progenitors, as well as markers indicative of either a biliary or hepatocyte fate (Figure S10b, Supporting Information). Moreover, markers characteristic of both intrahepatic and extrahepatic biliary epithelial cells were present in both constructs (Figure S10b, Supporting Information).

Further proteomic analysis revealed distinct protein profiles between CBD-like constructs cellularized with HuCCT1 cells versus those cellularized with cholangiocyte stem cells. Constructs containing HuCCT1 cells exhibited higher expression of proteins involved in actin cytoskeleton organization ($n = 79$) and vesicle-mediated transport ($n = 135$), whereas those containing cholangiocyte stem cells were enriched in proteins associated with small molecule metabolic processes ($n = 67$), nucleic acid metabolism ($n = 54$), and cellular respiration ($n = 15$) (Figure S10c, Supporting Information). These differences may explain the enhanced CLF export activity ($p < 0.05$) observed in constructs cellularized with cholangiocyte stem cells (Figure 11e). However, the lack of key bile acid transporters in these cells complicated the assessment of the constructs' bile modification abilities. Preliminary experiments showed slight, though non-significant, changes in Cl^-, carbon dioxide (CO_2), and calcium ion (Ca^{2+}) concentrations in bile samples exposed to the construct (Figure 11f). Under physiological conditions, biliary epithelial cells primarily contribute to bile modification through HCO_3^- secretion, typically coupled with Cl^- exchange. While direct quantification of HCO_3^- was not feasible, the observed increase in Cl^- and concurrent decrease in CO_2 levels suggest potential CFTR-mediated activity, given the inverse relationship between CO_2 and HCO_3^-.[100] Additionally, the reduction in Ca^{2+} levels in the processed bile may reflect active cellular uptake of Ca^{2+}, where it could serve as a second messenger to support the complex secretory and reabsorptive processes involved in bile modification.[33]

Collectively, these preliminary findings suggest that the CBD-like construct exhibits functional features reminiscent of biliary-like epithelium.

3. Discussion

This work aimed to establish the foundation for an implantable medical device to address the growing healthcare demand for CBD-related conditions, such as post-operative biliary strictures. Using established biofabrication methods, we created a tissue-engineered CBD-like construct that closely matches the size of native human tissue. The three-layer design, featuring ES-PCL encapsulated between two CollMA layers, offers distinct functional advantages over simpler bilayer systems. It enhances structural stability and compositional homogeneity, as demonstrated by the absence of delamination between the polymer layers, making the construct suitable for handling and surgical suturing. Beyond mechanical performance, this configuration may also support improved integration with host tissue. While the inner CollMA layer incorporates biliary epithelial cells that develop into a functional biliary-like epithelium, the outer, cell-free CollMA layer — offering a bioactive, cell-permissive interface — may play a key role in promoting host vascular integration. Once implanted, this layer may be colonized by vascular cells migrating from the para-choledochal arteries and veins surrounding the native ducts. Alternatively, it could be pre-vascularized with endothelial cells or progenitors to enhance integration. In contrast, bilayer constructs with a bare PCL outer surface may be less favorable, as PCL is bioinert and less likely to support interaction with surrounding tissues.

The CBD-like construct remained stable under physiological conditions, enabled bile flow without leakage, and exhibited bile acid transport and modification activities. In an ex vivo human blood assay, the construct's biomaterials elicited a favorable immune response, preventing excessive inflammation while promoting sustained EGF release, suggesting its potential to support tissue repair and integration. While the mechanism behind EGF upregulation remains unclear, evidence suggests the involvement of M2-polarized macrophages. We hypothesize that CollMA degradation promotes M2 polarization by generating amino acid signals. This is consistent with studies on acellular dermal matrices, where collagen degradation by macrophages activates an acid-sensing pathway involving Lamtor1, leading to M2 polarization and the expression of proregenerative signals, including EGF.[101]

Our approach followed a bottom-up strategy, beginning with the selection of biomaterials capable of supporting biliary epithelial cell reorganization and function, as well as providing the necessary mechanical properties. We focused on clinically-approved, degradable materials to minimize foreign body responses[20,102–104] and support host-mediated tissue remodeling. Ultimately, we selected collagen and PCL, which together offered a biocompatible substrate for biliary epithelial cell regeneration, as well as mechanical strength and durability.

Collagen was selected due to its abundance in CBD tissue[35] and widespread use in biliary tissue engineering.[16,30,105–110] While it provides essential molecular cues that support biliary epithelial cell adhesion, proliferation, and polarization, its native form often lacks the mechanical strength required for long-term

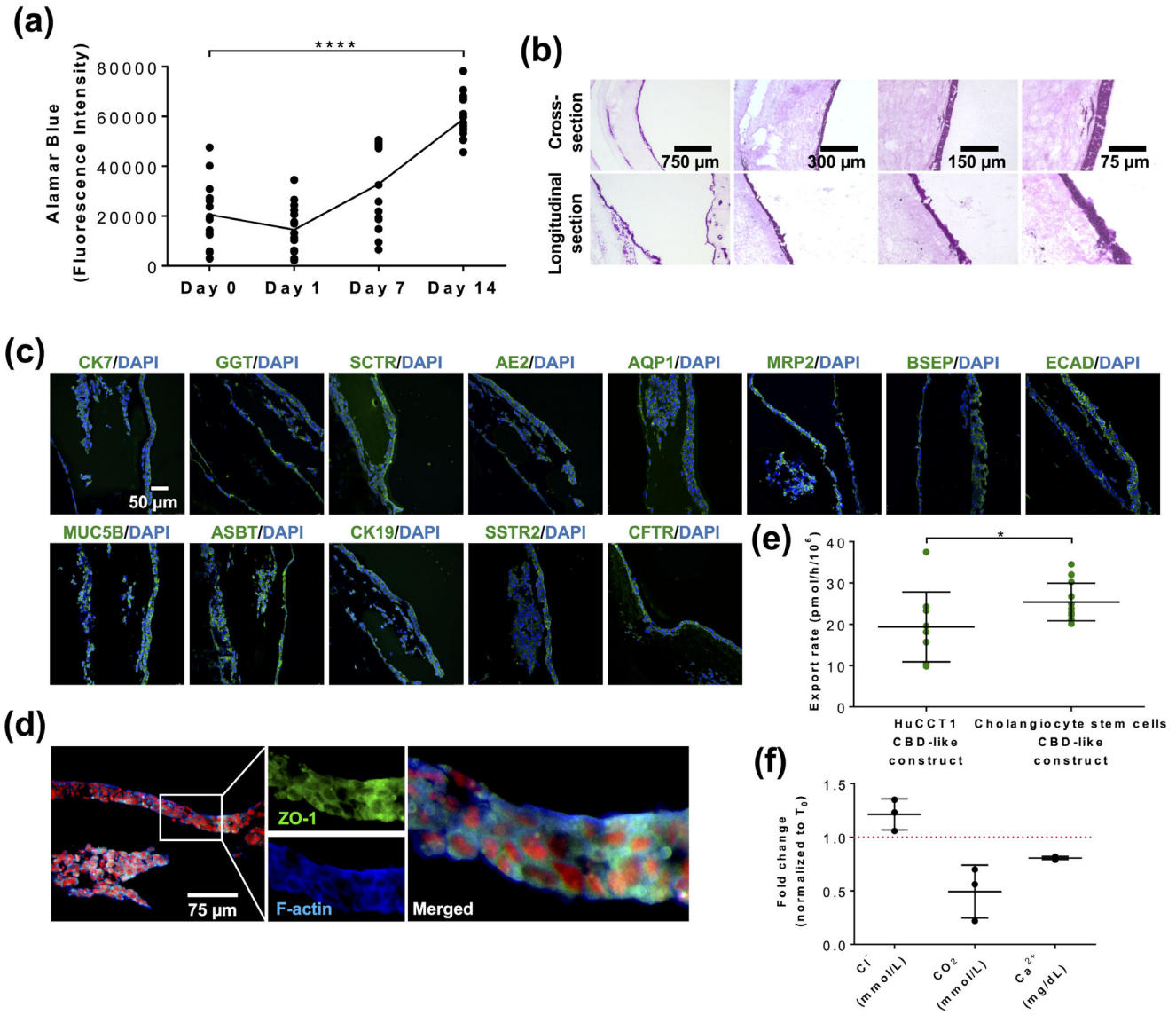

Figure 11. Cholangiocyte stem cell reorganization, marker expression, and function in the CBD-like construct. a) Graph of alamarBlue fluorescence intensity in the CBD-like construct cellularized with cholangiocyte stem cells (3 million cells/mL cells in 6 mgmL^{-1} CollMA) over the course of 14 days. Three tubes per time point were generated, each divided into five slices, for a total of 15 slices per time point subjected to alamarBlue assay. Each dot represents the fluorescence intensity of a tube slice. A mean line is shown. There is a significant increase at Day 14 compared to Day 0 (****, $p < 0.0001$, paired *t* test). b) Representative images of H&E-stained OCT compound-embedded cross and longitudinal sections of the cellularized CBD-like construct at Day 14 ($n = 3$). c) Representative confocal images of immunofluorescence staining of sections as in (b) for CK7, GGT, SCTR, AE2, AQP1, MRP2, BSEP, ECAD, MUC5B, ASBT, CK19, SSTR2, and CFTR (green). Nuclei were stained with DAPI (blue). d) Representative confocal images of immunofluorescence staining of sections as in (b) for ZO-1 (green) and F-actin (blue). Nuclei were stained with PI (red). Insets show apico-basal polarity and expression of F-actin in the surface epithelium. e) Rate of CLF export in CBD-like constructs cellularized with either HuCCT1 cells or cholangiocyte stem cells at Day 14, calculated by normalizing the amount of exported fluorescent dye against the number of cells in the construct (in millions) and elapsed time (in hours) for export. Data are presented as mean ± SD, with each dot representing a technical replicate (nine slices of the construct containing HuCCT1 cells and 12 slices of the construct containing cholangiocyte stem cells) from at least three independent experiments (*, $p < 0.05$, unpaired *t* test). f) Graph of relative Cl^-, CO_2, and Ca^{2+} levels in the bile exposed to the CBD-like construct cellularized with cholangiocyte stem cells (T_{20} normalized to T_0). Data are presented as mean ± SD, with each dot representing a technical replicate from an independent experiment ($n = 3$). Values above or below the red dot line indicate variations. No significant differences were observed between T_{20} and T_0 (Wilcoxon matched-pairs signed rank test).

use in engineered tissues. Sampaziotis et al., used densified collagen to create bile duct-like tubular scaffolds populated with primary human extrahepatic cholangiocyte organoids.[30] These scaffolds demonstrated regenerative potential in a mouse model of extrahepatic biliary injury, though questions remained regarding the extent of epithelial polarization and scaffold mechanical performance. In our approach, we used CollMA, a modified form of collagen in which free amines react with methacylate groups, enabling covalent crosslinking via a UV light-activated photoinitiator. This modification improves mechanical strength

and resistance to degradation, which is critical for in vivo applications where conditions such as bile exposure can accelerate collagen breakdown.[111,112] While UV light exposure is associated with genotoxic risk and oxidative DNA damage, UV-A is the least harmful of the three UV wavelengths.[113–115] Cell-laden constructs were exposed to UV-A for a short period, which we believe had minimal impact on cells, as suggested by similar cell behavior observed in both native and crosslinked collagen (data not shown). Future studies will assess DNA lesions, such as pyrimidine dimers, using assays such as the comet assay.[113] Importantly, UV-A-induced collagen crosslinking may not be essential, as the CBD-like construct also incorporates PCL, which is well-established for its stability and resistance to degradation.[116]

The combination of CollMA with the ES-PCL scaffold produced a multiphasic structure with a biological phase designed to integrate seamlessly with the host and remodel in vivo, and a mechanical phase providing temporary support during tissue regeneration. Although bilayered scaffolds incorporating PCL have been explored for biliary tissue engineering,[25,37] the specific combination of PCL and CollMA has, to the best of our knowledge, not been previously reported. Moreover, the integration of natural and synthetic polymers in hybrid scaffolds for biliary applications remains largely unexplored. Our fabrication strategy—combining PCL electrospinning, cell encapsulation in CollMA, and molding into a unified sequence tailored for biliary tissue engineering—represents a novel approach. The primary aim of this work was not to introduce new biomaterials, but to establish a streamlined, reproducible protocol using well-characterized materials. The comprehensive, multidisciplinary characterization of the resulting constructs—including material, biological, functional, and immunological assessments—highlights the rigor and innovation of our approach compared to existing studies. This detailed characterization not only affirms the construct's potential as an implantable device but also highlights its versatility as a platform for modeling development, studying diseases, and conducting drug screening tests.

While our strategy offers clear advantages, certain translational considerations remain. One concern is the use of bovine collagen, which may raise regulatory or immunogenicity issues. However, bovine collagen is already used in several FDA-approved applications, such as dermal fillers, shoulder implants, and anterior cruciate ligament implants (https://www.fda.gov/news-events/press-announcements/fda-authorizes- marketing-new-implant-repair-torn-acl).[117] If needed, recombinant human collagen could serve as an alternative for constructing the CBD-like construct.[118]

Other limitations include the choice of cell source, initial feasibility tests, and the sample size. Obtaining patient-derived primary extrahepatic biliary epithelial cells is particularly challenging, and while protocols exist for differentiating human induced pluripotent stem cells into biliary epithelial cells, none yield a mature, fully functional extrahepatic biliary epithelial cell population. The biliary epithelial cells induced by Dianat et al.[119] are compatible with small biliary epithelial cells, whereas those differentiated by Sampaziotis et al.[99] are more functionally aligned with large biliary epithelial cells, though they retain characteristics of intrahepatic biliary epithelial cells. Moreover, both methods result in cells with a phenotype that represents an intermediate stage between fetal and fully mature biliary cells. As a result, we relied on commercially available human biliary epithelial cell lines, which are easy to manipulate and expand. Unfortunately, many of the available biliary epithelial cell lines are derived from intrahepatic ducts and are cancerous. We initially optimized culture conditions using the intrahepatic cholangiocarcinoma HuCCT1 cell line, which was found to express markers compatible with large biliary epithelial cells, making them suitable for modeling extrahepatic biliary epithelium.

Due to logistical and cost constraints, we first optimized the culture conditions using flat disks before transitioning to tubular structures. HuCCT1 cells embedded in CollMA and molded into disks or tubes reorganized into a biliary-like epithelium. We used mass spectrometry-based proteomics to explore the mechanisms underlying this process. Our findings indicated that various cell-matrix and cell–cell interactions are involved. Compared to 2D cultures, HuCCT1 cells in CollMA disks downregulated major energy-consuming pathways, such as mitochondrial and RNA metabolism, likely to reduce ATP expenditure and support tissue remodeling, as evidenced by the increased levels of proteins involved in ECM deposition, modification, degradation, and organization. We hypothesize that an interplay between glycolysis, hypoxia, and oxidative stress response may contribute to ECM remodeling. Notably, ECM remodeling was not associated with EMT, suggesting HuCCT1 cells maintain their epithelial phenotype. Between Day 7 and Day 14, HuCCT1 cells in CollMA disks exhibited increased cell polarization, as evidenced by higher levels of proteins involved in non-canonical apical and basolateral trafficking. This signature of apico-basal polarization and ECM organization was even more pronounced in the complete CBD-like construct, which included the PCL-based mechanical phase.

To validate our CBD concept, we transitioned to commercially available cholangiocyte stem cells derived from healthy CBD.[99] While these cells are relatively easy to culture, they exhibit more limited growth potential compared to HuCCT1 cells. We performed proteomics to compare CBD-like constructs cellularized with either cell type, finding that tissue remodeling was more pronounced in constructs with HuCCT1 cells, likely due to their cancerous origin and greater plasticity. Future work will focus on using a more biologically relevant, patient-derived cell source. In clinical settings, autologous cell seeding could be considered; however, in certain situations, such as when personalized approaches are not feasible, when timing is limited, or in younger patients with greater regenerative capacity, an acellular CBD-like construct may offer advantages.

Another limitation was the number of technical replicates, particularly in proliferation, apoptosis, and functional assays. To increase the number of replicates, we sliced the tubes, a step that may introduce variability. However, viability and functional assays confirmed the overall reliability of our approach.

The CollMA tubular scaffold degraded progressively in bile, disappearing between Days 28 and 35, likely due to bile composition, pH, and enzymatic activity. In contrast, the ES-PCL tubular structure exhibited strong resistance to bile. It is worth noting that in vitro experiments involved continuous bile exposure, whereas in vivo, bile flows intermittently during digestion, meaning degradation may occur more slowly.

4. Conclusion and Future Directions

Tissue engineering and regenerative medicine aim to develop biological substitutes for repairing or replacing damaged bile ducts, which can lead to serious health complications and place a significant burden on healthcare systems. Plastic stents, often used as a first-line treatment for biliary stricture, require frequent replacements, while self-expanding metal stents offer longer patency but carry risks like migration and tissue ingrowth. Biodegradable scaffolds are a promising alternative, as they degrade naturally in the body, eliminating the need for replacement or removal. However, fine-tuning their degradation rate to match tissue regeneration remains a challenge, with risks of either inadequate support or chronic inflammation. Replicating the native bile duct's complex biological and mechanical properties is also a major hurdle.

We have successfully fabricated a multiphasic tubular structure that closely matches the size of the human native CBD, using two biocompatible biomaterials and biliary epithelial cells: one biomaterial supports biliary epithelial cell growth, while the other provides mechanical strength. Through extensive characterization—including histological and ultrastructural analyses, mechanical testing, biochemical assays, and mass spectrometry-based proteomics—we demonstrated the creation of a viable, functional biliary-like epithelium. The construct also exhibited homogeneity, stability, mechanical strength, handleability, suturability, and leak-free properties, making it a strong candidate for biliary tissue regenerative medicine.

Future studies will aim to incorporate a more biologically relevant biliary epithelial cell source, along with additional cells such as endothelial cells. Reconstructing both biliary and vascular networks is essential for enabling directional bile and blood flow. Vascularization strategies must account for anatomical variations in vascular supply across the CBD's supraduodenal, retroduodenal, retropancreatic, and intraduodenal segments,[34] and may draw on recent liver tissue engineering advances, such as bioprinted hierarchical vascular networks in microgel–hydrogel hybrid systems encapsulating high-density hepatocytes.[120] Further efforts will evaluate the construct's ability to withstand various mechanical forces, including fluid shear stress and hydrostatic pressure. Pre-clinical assessment in large animal models will follow. If proven safe and effective, this technology could offer new treatment options for CBD-associated diseases, reduce hospital admissions, and help lower overall healthcare costs.[121]

5. Experimental Section

Preparations of Biomaterials: PhotoCol-LAP Methacrylated Type I Collagen (ColIMA; Advanced Biomatrix, CA, USA) was prepared at an initial concentration of 8 $mgmL^{-1}$ following the manufacturer's instructions, and depending on the experiment, was diluted to 6 or 4 $mgmL^{-1}$. The ColIMA solution was supplemented with 0.18% v/v lithium phenyl-2,4,6-trimethylbenzoylphosphinate (LAP).[122]

PCL (MW 80000, Sigma–Aldrich, Germany) was dissolved in 1,1,1,3,3,3-Hexafluoro-2 propanol to form a 10% w/v solution.

Molding and Electrospinning Approach for the Biofabrication of a CBD-like Construct: To demonstrate the feasibility of the biofabrication process, a CBD-like construct was first fabricated using only biomaterials—ColIMA and PCL—employing molding and electrospinning techniques (Figure 1a,b; Video S1, Supporting Information).

A tubular-shaped mold was designed and fabricated using a computer-aided design software (SolidWorks Premium 2022 SP2.0) and 3D printing (EASY3D Shop Lab, Italy). The mold consists of four components (Figure 1b). First, it includes two half-hollow cylinders (hereinafter referred to as the mold's walls) with flat bases. These half-hollow cylinders can be combined to form an open-top hollow cylinder through a sliding closure system. The hollow cylinder has a height of 60 mm (excluding the base) and an inner diameter of 9 mm. The mold also contains a cylindrical stick (74 mm height, 5 mm diameter) that can be inserted inside the open-top cylinder. Finally, the mold is equipped with a removable cap featuring a pocket for the stick, ensuring alignment in the central position while also sealing the top of the hollow cylinder. When fully assembled, the mold produces a 60 mm long, 2 mm thick tubular CBD-like structure with a 5 mm inner diameter.

Electrospinning was employed to generate the ES-PCL tubular scaffold (Figure 1a). A stainless-steel rod with a diameter of 7 mm was used as a collecting target, which moved in both rotational and raster motion (30 mms^{-1}). A positive voltage of 15-kV was applied, and the PCL solution was drawn at a constant flow rate of 1.5 mL min^{-1} for 90 min. PCL fibers were collected on a grounded rotating (1850 rpm) mandrel, positioned 16 cm from the spinneret. After fabrication, the mandrel with the ES-PCL tubular scaffold was soaked in cold 70% v/v ethanol (−80 °C) for 5 min to facilitate scaffold removal. The scaffold was then washed with PBS, disinfected by immersion in 70% ethanol for 20 min, and rinsed three times with PBS for 30 min. The ES-PCL tubular scaffold was then inserted into the mold previously described, and a solution of ColIMA was poured between both the ES-PCL scaffold and the mold's stick, as well as between the ES-PCL scaffold and the mold's walls. The assembly was incubated at 37 °C for 15 min for thermal cross-linking. After incubation, the multiphasic tubular structure was removed from the mold's walls, leaving the central stick behind. The structure was photopolymerized using UV-A light exposure (using a LED-UV torch with emission wavelength of 395–400 nm, Brandson Equipment, Germany) for 2 min per side to achieve covalent cross-linking, initiated by LAP. The photopolymerized multiphasic tubular structure was then separated from the mold's stick, washed three times with PBS to remove excess unreacted LAP, and used for downstream applications. When cells were incorporated, they were added to the ColIMA solution before pouring it into the mold between the ES-PCL scaffold and the mold's stick. The space between the ES-PCL scaffold and the mold's walls was filled with a cell-free ColIMA solution. In this case, culture medium was used for the washes instead of PBS, and the cell-laden construct was cultured in a humidified incubator at 37 °C and 5% CO_2, with medium replacement every other day.

Microstructural Characterizations: To investigate the morphology and layer homogeneity of the cell-free CBD-like construct, SEM analyses were conducted. Briefly, samples ($n = 3$) were fabricated and frozen overnight at −80 °C. The samples were then lyophilized using the FreeZone Triad Cascade Benchtop Freeze Dryer (Labconco, MO, USA). During lyophilization, the shelf temperature followed a programmed sequence: −30 °C for 20 h, −10 °C for 1 h, 0 °C for 2 h, and 10 °C for 1 h and 30 min. Afterward, the samples were returned to room temperature. Throughout the process, the vacuum pressure was maintained at a constant 0.220 mbar, and the collector temperature remained at −80 °C. Once lyophilization was complete, the scaffolds were sectioned into three parts. These sections were then analyzed using the Phenom ProX Desktop SEM (Thermo Fisher Scientific, MA, USA).

Surface Morphology Characterizations: The outer surface morphology of the ES-PCL tubular scaffold ($n = 3$) was analyzed using the Phenom ProX Desktop SEM. Two images were captured per scaffold. A custom-made software, previously developed,[123] was then used to quantify the mean fiber diameter.

Uniaxial and Suture Retention Tests: The ES-PCL tubular scaffolds ($n = 9$), the cell-free CBD-like constructs ($n = 6$), and the cellularized CBD-like constructs ($n = 6$), underwent uniaxial testing using a tensile tester (Instron 68TM-10, MA, USA) equipped with a 500 N force transducer. Native porcine CBDs ($n = 9$) were used as controls. Briefly, porcine CBDs were sourced from a local slaughterhouse, rinsed in PBS to remove impurities, and prepared for analysis. Tests were performed in semi-dry conditions at room temperature. All samples were kept in a tubular shape and stretched at a constant speed of 2 $mmmin^{-1}$.[124]

Deformation was analyzed when the applied force exceeded 0.1 N.

Suture retention strength tests were conducted using the Instron 68TM-10 tester. The ES-PCL tubular scaffolds ($n = 9$) were cut into rectangular strips of 20 mm (axial) x 11 mm (circumferential) size. A 6-0 polypropylene monofilament suture (Covidien SURGIPRO II, Ireland) was used to create a single loop approximately 3 mm away from the scaffold's edge. The samples were then pulled at a rate of 1 mmmin^{-1} until the suture tore out.[27] The maximum force required to pull the suture through the sample was recorded as the suture retention strength.

Bile Leakage Assay: The permeability of both the ES-PCL scaffold and the cell-free CBD-like construct to bile was assessed using a custom-made perfusion system. A syringe pump (KD Scientific, MA, USA) connected to a 50 mL syringe (Multimedical, Italy) was used to deliver bile through tubing into the scaffolds ($n = 3$/group). Bile was harvested from the gallbladders of commercial pigs sourced from a local slaughterhouse and stored at −20 °C until needed. Bile was delivered at a physiological flow rate of 1.5 mL min^{-1}[24] for 10 min, at room temperature. Both the bile circulating within the scaffolds and any leaked bile were collected and weighed to estimate the leakage rate.

In Vitro Degradation Tests: The biodegradability and structural stability of the ES-PCL tubular scaffolds, the cell-free CollMA tubular scaffolds, and the cell-free CBD-like constructs ($n = 3$/group) were assessed after immersion in PBS or porcine bile (pH 7.38) at 37 °C, using a weight loss approach. Briefly, scaffolds were weighed immediately after the biofabrication process and at defined timed points during immersion. Before each weighing, samples were quickly dried using Kimtech Science Kimwipes (Kimberly-Clark Corporation, GA, USA). After each weighing, the samples were returned to the PBS or bile solution and placed back in a cell culture incubator. Measurements were taken initially every hour for 4 h, then daily for a week, and subsequently once a week until complete degradation occurred. Sample weights were plotted starting from Day 1,[125] when the samples showed their maximum swelling. The degradation rate was calculated as a percentage of residual weight (RW) using the following equation $RW\% = (W_t / W_0) * 100$, where W_0 is the initial weight of the sample just after biofabrication, and W_t was the weight at a specific time point.[126]

Whole Blood Cytokine Immunoassay: Venous blood was collected from three healthy donors (two males and one female, aged between 30 and 50 years) into K3EDTA tubes (Greiner Bio-One GmbH, Austria) at ISMETT Hospital, with exemption from Institutional Review Board (IRB) approval. The blood was diluted 1:4 in RPMI 1640 medium (Euroclone, Italy) supplemented with 1X penicillin/streptomycin (Sigma–Aldrich), 10 mM HEPES (Euroclone, Italy), and 1 mM L-glutamine (Euroclone), following the manufacturer's instructions. Slices of the cell-free CBD construct, each 0.5 cm in length, were incubated in the blood for 4 and 24 h at 37 °C and 5% CO_2. Untreated blood served as a negative control, while blood treated with 1 µgmL^{-1} of commercial LPS from *Escherichia coli* O111:B4 (Sigma–Aldrich) was used as a positive control. After incubation, supernatants were collected and stored at −80 °C until further analysis. Before testing, the samples were thawed, and the levels of selected cytokines, chemokines, and growth factors were quantified using the Invitrogen Cytokine 30-Plex Human Panel (Life Technologies, Germany), following the manufacturer's instructions.

Data were collected as mean fluorescence intensity (MFI) values and assessed for normality using the Shapiro-Wilk test. When normality was not met for a specific factor, such as MCP-1, a square root transformation was applied to normalize the data. Specifically, the Y values for each data point were transformed using the formula $Y = \sqrt{Y}$ to reduce skewness and approximate normality. No transformation was applied to the remaining factors that met the assumption of normality. For both transformed and untransformed data, a two-way analysis of variance (ANOVA) with multiple comparisons was performed to evaluate the effects of treatment, time, and their interaction. Specifically, cells within each row and column were compared to identify differences across experimental groups at each time point and condition. Post-hoc comparisons were then conducted using Tukey's test to identify which specific group means differed significantly from each other. Factors that changed significantly in the blood exposed to the construct compared to the control blood were graphed as transformed or untransformed values. Additionally, a heatmap of all cytokines was prepared, but it was presented using the means of the transformed values, regardless of the need for transformation, to maintain consistency.

Cell Culture: The ascites-derived HuCCT1 intrahepatic cell line was purchased from Creative Bioarray (NY, USA; Cat.No.: CSC-C9200W) and expanded in 2D culture in RPMI-1640 medium supplemented with 10% fetal bovine serum (Euroclone), 1X penicillin-streptomycin, 1X L-glutamine, and 1X MEM non-essential amino acid solution (Sigma-Aldrich), following the manufacturer's instructions. Cells were passaged when they reached about 90% confluency.

Human cholangiocyte stem cells derived from the CBD[99] were purchased from Celprogen (The Netherlands; Cat.No.: 36755-11) and expanded in 2D culture using Celprogen's expansion matrix and culture growth medium, according to the manufacturer's instructions. Cells were passaged when they reached about 70% confluency.

For marker characterization, cells were grown on chamber slides (Ibidi, Germany) and labeled with specific antibodies (Table S4, Supporting Information) using immunofluorescence staining, as described elsewhere.[127]

Both HuCCT1 cells and cholangiocyte stem cells were embedded in CollMA, as described below.

Cells were routinely tested for mycoplasma contamination using MycoStrip (InvivoGen, Italy) or VenorGeM OneStep (Minerva Biolabs, Germany).

Preparation of Cell-Laden CollMA Disks: Biliary epithelial cell-laden CollMA disks were fabricated as a toolkit to optimize culture conditions for efficient generation of a biliary-like epithelium. Three CollMA concentrations (4, 6, and 8 mgmL^{-1}) and three cell seeding densities (1, 3, and 5 million cells/mL) were tested. Briefly, 200 µL drops of the cell-CollMA mixture were placed onto 96- to 12-multiwell plates and photopolymerized under UV-A light for 2 min per side. The cell-laden CollMA disks were then incubated at 37 °C for 15 min to allow thermal crosslinking. Afterward, the disks were covered with culture medium and maintained in a humidified incubator at 37 °C, 5% CO_2 for up to 14 days (Figure S1, Supporting Information upper left panels). The culture medium was replaced every other day.

Cell viability, reorganization, function, and protein expression were evaluated in cell-laden CollMA disks under the different conditions, as described below and depicted in Figure S1 (Supporting Information) (upper right panels). All data were normalized to cell-free CollMA disks.

Preparation of Cell-Laden CollMA Tubular Scaffolds: A maximum of 3 mL of the optimized biliary epithelial cell-CollMA mixture (3 million cells/mL in 6 mgmL^{-1} CollMA) was poured into the tubular-shaped mold, and the mold with the solution was transferred to a cell culture incubator for 15 min to allow thermal cross-linking. The scaffold was then removed from the mold and exposed to UV-A light for 2 min per side, as previously described (Figure S1, Supporting Information, lower left panels). To maximize the number of technical replicates, each scaffold was cut with a scalpel into multiple slices of equal size. The slices were used to evaluate cell behaviors in the context of tubular systems, as opposed to the previously described flat disks. Analyses of cell viability, reorganization, and function were performed as for the disks and are further detailed in the following paragraphs (Figure S1, Supporting Information, lower right panels).

Assessment of Cell Metabolic Activity and Viability: Cell-laden CollMA disks or slices of the cellularized tubular scaffolds were incubated with the alamarBlue HS Cell Viability Reagent (Thermo Fisher Scientific) in multiwell plates and maintained in a humidified incubator at 37 °C, 5% CO_2 for 4 h. The fluorescence intensity, indicative of cell metabolic activity, was measured using the Spectrafluor Plus TECAN spectrometer (Switzerland) at an excitation wavelength of 535 nm and an emission wavelength of 595 nm.

Cell viability was also assessed using PI staining. Nuclei were stained using 4′,6-diamidino-2-phenylindole (DAPI, NucBlue Fixed Cell ReadyProbes Reagent, Thermo Fisher Scientific). A positive control of cell death was obtained by exposing cells to 70% ethanol for 30 min at room temperature. Cells were visualized using the EVOS M5000 microscope imaging system (Invitrogen, Thermo Fisher Scientific), and cell viability was estimated by dividing the number of live cells by the total number

of cells (five images per scaffold), counted using ImageJ software, version 1.53p (NIH, MD, USA; https://imagej.nih.gov/ij). The results were expressed as a percentage of living cells.

Assessment of Cell Reorganization: The reorganization of biliary epithelial cells in disks or tubular structures was investigated on Days 7 and 14 through histology and immunofluorescence staining. Briefly, both paraffin- and OCT-embedded sections were prepared. OCT compound was the embedding medium of choice when PCL was present to preserve its structure.

For histological assessment, sections were stained with Hematoxylin (Harris' Hematoxylin, Bio Optica, Italy) and Eosin (Eosin Y disodium salt, Sigma–Aldrich) (H&E), following the manufacturer's instructions. Images were captured using the EVOS M5000.

For immunofluorescence staining, paraffin-embedded sections were deparaffinized with xylenes (or Histo-Clear by National Diagnostics, GA, USA, if ES-PCL was present[128]) and rehydrated through graded alcohols and water. Rehydrated sections underwent heat-induced epitope retrieval using 10 mM Sodium citrate, 0.05% v/v Tween 20, pH 6.0. This was followed by bovine serum albumin blocking, and the sections were incubated with primary antibodies (Table S4, Supporting Information) overnight at 4 °C. The next day, the sections were incubated with Alexa Fluor 488 or 594-conjugated secondary antibodies (Thermo Fisher Scientific) for 1 h at room temperature. Cell nuclei were stained with DAPI.

Immunofluorescence staining of OCT compound-embedded sections was performed as previously described.[127]

Stained sections were visualized with a confocal microscope (Leica TCS SP5 II, Germany). Sections of the cell-free CollMA scaffolds were stained in parallel and used as controls to adjust for background noise. Since the image brightness appeared reduced after exporting to PowerPoint, it was uniformly adjusted for all samples to maintain consistent visualization without altering data integrity. Fluorescence intensity for each marker was measured from confocal images (five images/marker/experiment) as an integrated density (IntDen) using ImageJ, as previously described.[129]

Assessment of Cell Function: The ability of biliary epithelial cells in disks or tubular structures to transport bile acids was assessed using the fluorescein-labeled bile acid analog CLF (1.5 µM; Corning Incorporated, NY, USA). FITC (1.5 µM; Sigma–Aldrich) was used as a control. Cell-free scaffolds were also included in the experiment and were treated with FITC as controls. Following a 30-min incubation with either CLF or FITC (uptake phase), all samples were washed three times in RPMI-1640 medium without phenol red and maintained in this medium for 2 h to allow the export, if any, of the molecules absorbed.

To estimate the degree of export, medium aliquots were collected immediately after the washes (T_0), and again after 2 h (T_2). Fluorescence signals were measured in these aliquots using the TECAN SPECTRAFluor Plus microplate reader set to 485 nm excitation and 585 nm emission wavelengths. Functional biliary epithelial cells can export CLF owing to the expression of specific transporters on their cell membranes, whereas they cannot export FITC.[52] Any change in the FITC fluorescent signal in T_2 samples with respect to T_0 is considered background noise.

Relative quantification of exported CLF was obtained using the equation: $\boldsymbol{CLF_{rel\ exp} = (CLF_{T2} - CLF_{T0}) - [(FITC_{T2} - FITC_{T0}) - (cell\text{-}free\ scaffold\ FITC_{T2} - cell\text{-}free\ scaffold\ FITC_{T0})]}$. Absolute quantification of exported CLF ($\boldsymbol{CLF_{abs\ exp}}$) was obtained using a standard curve constructed with known CLF amounts. Finally, the CLF export rate was calculated considering the incubation period in hrs ($\boldsymbol{IP_h}$) and the number of cells in millions ($\boldsymbol{N_m}$) using the equation: $\boldsymbol{CLF_{exp\ rate} = (CLF_{abs\ exp} / IP_h) / N_m}$.

Microscopic images were captured during both the uptake and export phases using the EVOS M5000.

Sample Processing and Mass Spectrometry (MS) Analysis: Two different datasets were generated and analyzed. The first dataset contained HuCCT1 cell-laden CollMA disks at Day 7, HuCCT1 cell-laden CollMA disks at Day 14, HuCCT1 cells in 2D culture ($n = 6$/group), and cell-free CollMA disks ($n = 3$). The second dataset contained HuCCT1 cell-laden CollMA disks at Day 14, CBD-like constructs at Day 14 containing either HuCCT1 cells or cholangiocyte stem cells ($n = 6$/group), and cell-free CollMA disks and CBD-like constructs ($n = 3$/group).

All samples were lysed for 10 min at 4 °C using STET buffer (50 mM Tris, pH 7.5, 150 mM NaCl, 2 mM EDTA, 1% v/v Triton) containing cOmplete, EDTA-free Protease Inhibitor Cocktail (Roche, Switzerland). Proteins were purified from the lysates by centrifugation at maximum speed for 5 min at 4 °C and quantified using the T-Pro BCA Protein Assay Kit (TWIN HELIX, Italy) on a TECAN Spark Multi-Mode Microplate Reader, following the manufacturer's instructions.

An equal amount of protein from each sample was subjected to filter-aided sample preparation (FASP) using 10 kDa Vivacon 500 spin filters (Sartorius, Germany).[130] Briefly, proteins were reduced with 20 mM dithiothreitol for 30 min at 37 °C, and free cysteine residues were alkylated with 50 mM iodoacetamide (Sigma–Aldrich) for 5 min at room temperature in the dark. After three washes with 100 mM Tris-HCl/8 M urea, pH 8.0, proteins were digested with 0.2 µg LysC (Promega, Italy) in 25 mM Tris-HCl/2 M urea for 16 h at 37 °C, followed by a second digestion with 0.2 µg trypsin in 50 mM ammonium bicarbonate (Promega) for 4 h at 37 °C. The peptides were eluted into collection tubes and acidified with 0.1% v/v formic acid in H_2O (Sigma–Aldrich). Peptides were therefore desalted by stop-and-go extraction with self-packed Empore C18 membrane tips (CDS Analytical, PA, USA)[131] and eluted using 60% v/v acetonitrile/40% H_2O containing 0.1% v/v formic acid (Sigma–Aldrich). After vacuum centrifugation, the peptides were concentrated and dissolved in 20 µl 0.1% v/v formic acid in H_2O. Peptide concentrations were quantified using Nanodrop 2000 (Thermo Fisher Scientific).

For the first dataset, a total of 1.2 µg of protein per sample was loaded onto a Thermo Fisher Scientific Dionex UltiMate 3000 RSLCnano UHPLC system, which was coupled online via a Nanospray Flex Ion Source (Thermo Fisher Scientific) to a Q Exactive mass spectrometer (Thermo Fisher Scientific). Peptides were separated on an Acclaim PEPMap C18 column (50 cm × 75 µm ID, Thermo Fisher Scientific) with 250 nLmin^{-1} flow using a binary gradient of water and acetonitrile supplemented with 0.1% formic acid. Data-dependent acquisition (DDA) discovery was used for label-free quantification (LFQ). Full MS scans were acquired at a resolution of 70000, with a scan range of 300–1400 *m/z*, an automatic gain control (AGC) target of 1E+6, and a max injection time of 50 ms. The DDA was applied to the ten most intense peptide ions per full MS scan for peptide fragmentation (resolution: 17500; isolation width: 2 *m/z*; AGC target: 1E+5; normalized collision energy: 25%; max injection time: 120 ms). A dynamic exclusion of 120 s was used for peptide fragmentation.

The second dataset was analyzed using a Vanquish Neo nanoLC system (Thermo Scientific) coupled online with an Exploris 480 mass spectrometer (Thermo Fischer Scientific) and data-independent acquisition (DIA). This workflow was used to enhance the detection of low-abundant proteins, which might be masked by CollMA and other high-abundance proteins. Samples were processed by FASP and stop-and-go extraction, as described above. Eluted peptides were loaded onto an Acclaim PEPMap C18 column (25cm × 75 µm ID, Thermo Scientific). Peptides were separated using a 130 min binary gradient of water and acetonitrile containing 0.1% formic acid. Data-independent acquisition was performed using a full MS1 scan (400 *m/z* to 1200 *m/z*) followed by 60 sequential windows with an overlap of 1 *m/z* and window placement optimization enabled. Full scans were acquired at a 120000 resolution, 3×10^6 AGC, and 50 ms maximum injection time. The 60 isolation windows were scanned with a 30000 resolution, 8×10^5 AGC, and a maximum injection time set to auto to achieve the optimal cycle time. Fragmentation was induced with a normalized collision energy set at 30%.

Proteomics Data Analysis: The peptide report output from DDA discovery (first dataset) was analyzed using MaxQuant software, version 2.0.1.0 (maxquant.org, Max-Planck Institute, Germany). The MS data were searched against a reviewed + canonical FASTA database for *Homo sapiens*. Trypsin/P was defined as a protease, and two missed cleavages were allowed for the database search. The "first search" option was used to recalibrate the peptide masses within a window of 20 ppm. For the main search, peptide and peptide fragment mass tolerances were set to 4.5 and 20 ppm, respectively. Carbamidomethylation of cysteine was defined as a static modification, while protein N-terminal acetylation and methionine oxidation were set as variable modifications. The "match between runs" option was enabled with a 1.5 min match time window. LFQ of proteins

required at least two ratio counts of unique peptides. Unique and razor peptides were used for quantification, with normalization allowed.

Bovine CollMA was used to provide human biliary epithelial cells with a physical support. Due to the challenges of unambiguous species determination of the collagen proteins in the protein lysates—complicated by both the repetitiveness of the collagen sequence pattern and the extreme conservation of the sequence—the peptide report output from DIA discovery (second dataset) was analyzed using DIA-NN software, version 1.8.1. This analysis used a predicted library generated from an in silico-digested human UniProt Reference database, customized by adding the bovine Col1a1 entry (P02453|CO1A1_BOVIN), and involving cuts at K* and R*. Two missed cleavages were allowed, and the minimal peptide length was set to 6. This search strategy enabled the removal of Col1a1 peptides derived from the scaffold.

Bioinformatic Analysis of Proteomics Data: LFQ data from both the DDA discovery (first dataset) and the DIA discovery (second dataset) were processed in Perseus, version 1.6.13.0, for statistical analysis. LFQ values were Log2-transformed, and proteins were considered present only if they had a valid LFQ value in at least three biological replicates/group. Log2 fold changes (FC) were calculated, and a two-sided Student's *t* test was used to determine statistical significance. With the exception of data presented in Figure S6a,b, (Supporting Information) changes in protein abundance were arbitrarily considered statistically significant and biologically relevant when they met the following criteria: P value ≤ 0.05 [i.e., -Log10 (P value) ≥ 1.3], and log2FC ≥ 1 or log2FC ≤ -1. Volcano plots were generated using GraphPad Prism, version 10, and were used to summarize the results of the differential analysis.

Both the STRING database, version 11.5, and FunRich, version 3.1.4, were used to construct protein–protein interaction (PPI) networks and perform GO and Kyoto Encyclopedia of Genes and Genomes (KEGG) pathway enrichment analyses.

Bile Modification Assay: To investigate the ability of CBD-like constructs to modify the bile, constructs at Day 14 ($n = 3$) were exposed to porcine bile, which was retrieved and stored as previously described. Prior to the test, the bile was centrifuged at maximum speed for 5 min to remove debris. After three washes with PBS, each construct was incubated with 1 mL of bile. A 500 µL aliquot was immediately retrieved and frozen at 20 °C, serving as the baseline sample (T_0). A second 500 µL aliquot was collected from each construct 20 min after incubation (T_{20}) and frozen as before. The concentrations of Cl^-, CO_2, and Ca^{2+} were measured in T_0 and T_{20} bile aliquots using the Dimension Vista 1500 Intelligent Lab System (Siemens Healthcare, Germany) and the V-LYTE Fluids K820, K825, K1137, and K1023, following the manufacturer's instructions. The levels of analytes are presented as fold changes (T_{20} vs T_0).

Statistical Analysis: Statistical analyses were performed using GraphPad Prism, version 6.0 and 10.4.1. Data were presented as individual values or mean ± SD, as described in the figure legends. Group sizes (n) were indicated in the corresponding experimental sections and were reiterated in the figure legends, along with the statistical test applied.

The experiments were not randomized, and investigators were not blinded during the experiments.

Supporting Information

Supporting Information is available from the Wiley Online Library or from the author.

Acknowledgements

This work was supported by the Ri.MED Foundation and the Sicilian Region (European Regional Development Fund – PO FESR 2014/2020 – Azione 1.1.5 – Progetto PROMETEO). The authors would like to thank: Dr. Augustin Lerebours from Visy, Chavanod, France, for mold designing; Francesco Paolo Bonomo from Advanced Technologies Network Center, Palermo, Italy, for help with SEM acquisitions; Dr. Marzio Di Giuseppe from Ri.MED's Cardiovascular Tissue Engineering group, for help with mechanical characterizations; Dr. Laura Modica de Mohac, from Ri.MED's Cardiovascular Tissue Engineering group, for PCL preparation and electrospinning; Prof. Gaetano Burriesci and Dr. Danila Vella from Ri.MED's Bioengineering group, for support with mold fabrication; Dr. Valeria Pagano and Nazareno Costa from Ri.MED's Animal Welfare unit, for the retrieval of porcine CBDs and bile from a local slaughterhouse; Anna Paola Carreca and Margot Lo Pinto, from Ri.MED's Proteomics group, for mass spectrometry sample preparations; Dr. Claudia Coronnello from Ri.MED's Advanced Data Analysis group, for support on statistical analysis; Prof. Massimo Pinzani for insightful discussions; Claudio Catalano, Marika Gallina, and Ruben Leone, students at the I.T.S. Academy New Life Technologies "Alessandro Volta", Palermo, Italy, for help with immunofluorescence stainings and for recording the video illustrating the procedure; Daniele Galvagno from Ri.MED purchasing office for assistance with lab supply ordering; Ri.MED's technicians and supporting staff based in ISMETT; Dr. Daniele Di Carlo and Mario Sorrentino from ISMETT's Diagnostic Laboratories, for support with bile biochemical characterization; Dr. Rosa Liotta, Giovanna Fleres, Francesca Sciabica, and Elizabeta Iliovska, from ISMETT's Pathology Service, for support in histology tissue processing. Finally, the authors would like to thank ISMETT for access to shared laboratories and equipment.

Conflict of Interest

The authors declare no conflict of interest.

Author Contributions

M.G.F. conceived the study. M.G.F. and M.P. designed the experiments. M.P., M.B., M.C., D.P., and R.B. performed experiments. M.P., M.G.F., M.B., and M.C. analyzed the experiments. M.G.F. and M.P. wrote the manuscript. R.D.G. and A.D. provided intellectual feedback. S.G. supervised D.P., S.D.S. supervised M.C. All authors have read and approved the manuscript.

Data Availability Statement

The data that support the findings of this study are available from the corresponding author upon reasonable request.

Keywords

biliary system, common bile duct, electrospinning, hydrogels, stricture, tissue engineering

Received: March 31, 2025
Revised: May 26, 2025
Published online: June 16, 2025

[1] M. Strazzabosco, L. Fabris, C. Spirli, *J. Clin. Gastroenterol.* **2005**, *39*, S90.
[2] K. P. Croome, A. K. Mathur, B. Aqel, L. Yang, T. Taner, J. K. Heimbach, C. B. Rosen, R. Paz-Fumagalli, C. B. Taner, *Transplantation* **2022**, *106*, 1206.
[3] J. Eden, R. X. Sousa Da Silva, M. Cortes-Cerisuelo, K. Croome, R. De Carlis, A. J. Hessheimer, X. Muller, F. de Goeij, V. Banz, G. Magini, P. Compagnon, A. Elmer, A. Lauterio, R. Panconesi, J. Widmer, D. Dondossola, P. Muiesan, D. Monbaliu, M. de Rosner van Rosmalen, O. Detry, C. Fondevila, I. Jochmans, J. Pirenne, F. Immer, G. C. Oniscu, J. de Jonge, M. Lesurtel, L. G. De Carlis, C. B. Taner, N. Heaton, et al., *J. Hepatol.* **2023**, *78*, 1007.

[4] T. Jiang, C. Li, B. Duan, Y. Liu, L. Wang, S. Lu, *Ann. Hepatol.* **2016**, *15*, 41.
[5] F. Yuan, E. D. Saunders, J. McDonald, A. Balar, J. Pence, C. K. Brady, M. Hutchison, R. Grammer, *Dig. Dis. Interv.* **2022**, *06*, 174.
[6] M. Y. Wong, P. Saxena, A. J. Kaffes, *Diagnostics (Basel, Switzerland)* **2020**, *10*.
[7] J.-M. Dumonceau, A. Tringali, I. S. Papanikolaou, D. Blero, B. Mangiavillano, A. Schmidt, G. Vanbiervliet, G. Costamagna, J. Devière, J. García-Cano, T. Gyökeres, C. Hassan, F. Prat, P. D. Siersema, J. E. van Hooft, *Endoscopy* **2018**, *50*, 910.
[8] N. J. Sissingh, B. A. de Vries, A. Inderson, B. van Hoek, F. van der Heide, J. E. van Hooft, *Gastrointest. Endosc.* **2023**, *97*, 704.
[9] R. Andersson, K. Eriksson, P.-J. Blind, B. Tingstedt, *HPB* **2008**, *10*, 416.
[10] P. G. van Boeckel, F. P. Vleggaar, P. D. Siersema, *BMC Gastroenterol.* **2009**, *9*, 96.
[11] R. Lam, T. Muniraj, *World J. Gastroenterol.* **2021**, *27*, 6357.
[12] S. Nennstiel, A. Weber, G. Frick, B. Haller, A. Meining, R. M. Schmid, B. Neu, *J. Clin. Gastroenterol.* **2015**, *49*, 764.
[13] R. S. Kadaba, K. A. Bowers, S. Khorsandi, R. R. Hutchins, A. T. Abraham, S.-J. Sarker, S. Bhattacharya, H. M. Kocher, *Ann. R. Coll. Surg. Engl.* **2017**, *99*, 210.
[14] G. Mauri, C. Michelozzi, F. Melchiorre, D. Poretti, V. Pedicini, M. Salvetti, E. Criado, J. Falcò Fages, M. Á. De Gregorio, A. Laborda, L. M. Sonfienza, G. Cornalba, L. Monfardini, J. Panek, T. Andrasina, M. Gimenez, *Eur. Radiol.* **2016**, *26*, 4057.
[15] A. W. Justin, K. Saeb-Parsy, A. E. Markaki, L. Vallier, F. Sampaziotis, *Biochim. Biophys. Acta – Mol. Basis Dis.* **2018**, *1864*, 1532.
[16] Q. Sun, Z. Shen, X. Liang, Y. He, D. Kong, A. C. Midgley, K. Wang, *Materials (Basel)* **2021**, *14*, 7468.
[17] L. Tao, Q. Li, H. Ren, B. Chen, X. Hou, L. Mou, S. Zhou, J. Zhou, X. Sun, J. Dai, Y. Ding, *Artif. Organs* **2015**, *39*, 352.
[18] A. J. Pérez Alonso, C. Del Olmo Rivas, I. M. Romero, F. J. Cañizares Garcia, P. T. Poyatos, *J. Surg. Res.* **2013**, *179*, 18.
[19] S. Nakashima, T. Nakamura, K. Miyagawa, T. Yoshikawa, S. Kin, Y. Kuriu, Y. Nakase, C. Sakakura, E. Otsuji, A. Hagiwara, H. I. Yamagishi, *Int. J. Artif. Organs* **2007**, *30*, 75.
[20] D. S. Mendelowitz, J. M. Beal, *Am. J. Surg.* **1982**, *143*, 221.
[21] M. Aikawa, M. Miyazawa, K. Okamoto, Y. Toshimitsu, K. Okada, N. Akimoto, Y. Ueno, I. Koyama, Y. Ikada, *J. Gastrointest. Surg.* **2012**, *16*, 529.
[22] Y.-L. Liang, Y.-C. Yu, K. Liu, W.-J. Wang, J.-B. Ying, Y.-F. Wang, X.-J. Cai, *World J. Gastroenterol.* **2012**, *18*, 5205.
[23] M. Rosen, J. Ponsky, R. Petras, A. Fanning, F. Brody, F. Duperier, *Surgery* **2002**, *132*, 480.
[24] X. Jiang, X. Xiong, Y. Lin, Y. Lu, J. Cheng, N. Cheng, J. Zhang, *Acta Biomater.* **2022**, *150*, 238.
[25] M. Miyazawa, T. Torii, Y. Toshimitsu, K. Okada, I. Koyama, Y. A. Ikada, *Am. J. Transplant* **2005**, *5*, 1541.
[26] C. Zong, M. Wang, F. Yang, G. Chen, J. Chen, Z. Tang, Q. Liu, C. Gao, L. Ma, J. Wang, *J. Tissue Eng. Regener. Med.* **2017**, *11*, 966.
[27] J. Yan, X. Liu, J. Liu, X. Zhang, Q. Zheng, J. Nan, M. Lin, H. Pan, Y. Wang, X. Cai, J. Yin, *Mater. Des.* **2021**, *212*, 110229.
[28] E. M. Buisson, S.-H. Park, M. Kim, K. Kang, S. Yoon, J. E. Lee, Y. W. Kim, N. K. Lee, M. A. Jeong, B.-K. Kang, S. B. Lee, V. M. Factor, D. Seo, H. Kim, J. Jeong, H. J. Kim, D. Choi, *Bioeng. Transl. Med.* **2022**, *7*, 10252.
[29] C. Chen, P. G. M. Jochems, L. Salz, K. Schneeberger, L. C. Penning, S. F. J. van de Graaf, U. Beuers, H. Clevers, N. Geijsen, R. Masereeuw, B. Spee, *Biofabrication* **2018**, *10*, 034103.
[30] F. Sampaziotis, A. W. Justin, O. C. Tysoe, S. Sawiak, E. M. Godfrey, S. S. Upponi, R. L. Gieseck, M. C. de Brito, N. L. Berntsen, M. J. Gómez-Vázquez, D. Ortmann, L. Yiangou, A. Ross, J. Bargehr, A. Bertero, M. C. F. Zonneveld, M. T. Pedersen, M. Pawlowski, L. Valestrand, P. Madrigal, N. Georgakopoulos, N. Pirmadjid, G. M. Skeldon, J. Casey, W. Shu, P. M. Materek, K. E. Snijders, S. E. Brown, C. A. Rimland, I. Simonic, et al., *Nat. Med.* **2017**, *23*, 954.
[31] M. G. Worku, E. F. Enyew, Z. T. Desita, A. M. Moges, *PLoS One* **2020**, *15*, 0227135.
[32] E. Girard, G. Chagnon, E. Gremen, M. Calvez, C. Masri, J. Boutonnat, B. Trilling, B. Nottelet, *J. Mech. Behav. Biomed. Mater.* **2019**, *98*, 291.
[33] J. H. Tabibian, A. I. Masyuk, T. V. Masyuk, S. P. O'Hara, N. F. P. C. LaRusso, *Compr. Physiol.* **2013**, *3*, 541.
[34] C. S. Ramesh Babu, M. Sharma, *J. Clin. Exp. Hepatol.* **2014**, *4*, S18.
[35] B. U. Duch, H. L. Andersen, J. Smith, G. S. Kassab, H. Gregersen, *Neurogastroenterol. Motil.* **2002**, *14*, 111.
[36] H. Lu, K. Zhang, J. Yi, A. Wei, *Int. J. Concr. Struct. Mater.* **2022**, *16*, 24.
[37] M. Miyazawa, M. Aikawa, K. Okada, Y. Watanabe, K. Okamoto, S. Santosh, S. Yamaguchi, I. Koyama, Y. Ikada, *Int. Surg.* **2015**, *100*, 1408.
[38] K. Tamada, T. Tomiyama, A. Oohashi, T. Aizawa, T. Nishizono, S. Wada, S. Tano, T. Miyata, Y. Satoh, K. Ido, K. Kimura, *Gastrointest. Endosc.* **1999**, *49*, 199.
[39] S. J. Schulte, R. L. Baron, S. A. Teefey, C. A. Rohrmann, P. C. Freeny, W. P. Shuman, M. A. Foster, *Am. J. Roentgenol.* **1990**, *154*, 79.
[40] W. C. Li, H. M. Zhang, J. Li, R. K. Dong, B. C. Yao, X. J. He, H. Q. Wang, J. Song, *Transplant. Proc.* **2013**, *45*, 741.
[41] X. Meng, X. Wang, Y. Jiang, B. Zhang, K. Li, Q. Li, *RSC Adv.* **2019**, *9*, 21258.
[42] G. C. Miceli, F. S. Palumbo, F. P. Bonomo, M. Zingales, M. Licciardi, *Polymers* **2022**, *14*, 4486.
[43] S. L. Deshmane, S. Kremlev, S. Amini, B. E. Sawaya, *J. Interf. Cytokine Res.* **2009**, *29*, 313.
[44] T. J. Schall, K. Bacon, K. J. Toy, D. V. Goeddel, *Nature* **1990**, *347*, 669.
[45] J. T. Tan, E. Dudl, E. LeRoy, R. Murray, J. Sprent, K. I. Weinberg, C. D. Surh, *Proc. Natl. Acad. Sci.* **2001**, *98*, 8732.
[46] P.-R. Burgel, J. A. Nadel, *Eur. Respir. J.* **2008**, *32*, 1068.
[47] T. Lan, S. Qian, C. Tang, J. Gao, *Front. Immunol.* **2022**, *13*, 866040.
[48] C. J. Soroka, J. L. Boyer, *Mol. Aspects Med.* **2014**, *37*, 3.
[49] J. A. Tunggal, I. Helfrich, A. Schmitz, H. Schwarz, D. Günzel, M. Fromm, R. Kemler, T. Krieg, C. M. Niessen, *EMBO J.* **2005**, *24*, 1146.
[50] D. W. Kufe, *Nat. Rev. Cancer* **2009**, *9*, 874.
[51] J. A. Barber, S. H. Stahl, C. Summers, G. Barrett, B. Kevin Park, J. R. Foster, J. Gerald Kenna, *Toxicol. Sci.* **2015**, *148*, 48.
[52] S. Feng, J. Wu, W. L. Qiu, L. Yang, X. Deng, Y. Zhou, Y. Chen, X. Li, L. Yu, H. Li, Z. R. Xu, Y. Xiao, X. Ren, L. Zhang, C. Wang, Z. Sun, J. Wang, X. Ding, Y. Chen, P. Gadue, G. Pan, M. Ogawa, S. Ogawa, J. Na, P. Zhang, L. Hui, H. Yin, L. Chen, C. R. Xu, X. Cheng, *Cell Rep.* **2020**, *33*, 108455.
[53] O. Haller, P. Staeheli, G. Kochs, *Biochimie* **2007**, *89*, 812.
[54] O. Haller, G. Kochs, *Traffic* **2002**, *3*, 710.
[55] K. Ringer, J. Riehl, M. Müller, J. Dewes, F. Hoff, R. Jacob, *Traffic* **2018**, *19*, 947.
[56] D. J. Lenschow, C. Lai, N. Frias-Staheli, N. V. Giannakopoulos, A. Lutz, T. Wolff, A. Osiak, B. Levine, R. E. Schmidt, A. García-Sastre, D. A. Leib, A. Pekosz, K. P. Knobeloch, I. Horak, H. W. Virgin IV, *Proc. Natl. Acad. Sci. USA* **2007**, *104*, 1371.
[57] F. Gugliesi, M. Bawadekar, M. de Andrea, V. Dell'Oste, V. Caneparo, A. Tincani, M. Gariglio, S. Landolfo, *PLoS One* **2013**, *8*, 63045.
[58] Y. C. Perng, D. J. Lenschow, *Nat. Rev. Microbiol.* **2018**, *16*, 423.
[59] H. S. Kulkarni, M. L. Elvington, Y. C. Perng, M. K. Liszewski, D. E. Byers, C. Farkouh, R. D. Yusen, D. J. Lenschow, S. L. Brody, J. P. Atkinson, *Am. J. Respir. Cell Mol. Biol.* **2019**, *60*, 144.
[60] C. Fang, T. D. Manes, L. Liu, K. Liu, L. Qin, G. Li, Z. Tobiasova, N. C. Kirkiles-Smith, M. Patel, J. Merola, W. Fu, R. Liu, C. Xie, G. T. Tietjen,

P. A. Nigrovic, G. Tellides, J. S. Pober, D. Jane-wit, *Nat. Commun.* **2019**, *10*, 2247.
[61] A. E. Mammel, K. C. Delgado, A. L. Chin, A. F. Condon, J. Q. Hill, S. A. Aicher, Y. Wang, L. M. Fedorov, F. L. Robinson, *Hum. Mol. Genet.* **2022**, *31*, 1216.
[62] J. Winkler, A. Abisoye-Ogunniyan, K. J. Metcalf, Z. Werb, *Nat. Commun.* **2020**, *11*, 5120.
[63] S. Fulda, A. M. Gorman, O. Hori, A. C. Samali, *Int. J. Cell Biol.* **2010**, *2010*.
[64] R. J. Haines, L. C. Pendleton, D. C. Eichler, *Int. J. Biochem. Mol. Biol.* **2011**, *2*, 8.
[65] J. H. M. van der Meer, R. J. de Boer, B. J. Meijer, W. L. Smit, J. L. M. Vermeulen, S. Meisner, M. van Roest, P. J. Koelink, E. Dekker, T. B. M. Hakvoort, J. Koster, L. J. A. C. Hawinkels, J. Heijmans, E. A. Struijs, M. A. Boermeester, G. R. van den Brink, V. Muncan, *Cell Death Dis.* **2021**, *12*, 897.
[66] A. Ghanem, A. Kitanovic, J. Holzwarth, S. Wölfl, *Microb. Cell* **2017**, *4*, 52.
[67] P. B. Talbert, S. Henikoff, *J. Cell Sci.* **2021**, *134*, jcs244749.
[68] L. Scaramuzzino, V. Lucchino, S. Scalise, M. Lo Conte, C. Zannino, A. Sacco, G. Cuda, *Cells* **2021**, *10*, 2431.
[69] S. Ruijtenberg, S. van den Heuvel, *Cell Cycle* **2016**, *15*, 196.
[70] M. Pathan, S. Keerthikumar, C. S. Ang, L. Gangoda, C. Y. J. Quek, N. A. Williamson, D. Mouradov, O. M. Sieber, R. J. Simpson, A. Salim, A. Bacic, A. F. Hill, D. A. Stroud, M. T. Ryan, J. I. Agbinya, J. M. Mariadason, A. W. Burgess, S. Mathivanan, *Proteomics* **2015**, *15*, 2597.
[71] L. Albacete-Albacete, M. Sánchez-Álvarez, M. A. del Pozo, *Front. Immunol.* **2021**, *12*, 671485.
[72] S. Varma, J. P. R. O. Orgel, J. D. Schieber, *Int. J. Mol. Sci.* **2021**, *22*, 9068.
[73] Y. Chen, M. Terajima, Y. Yang, L. Sun, Y. H. Ahn, D. Pankova, D. S. Puperi, T. Watanabe, M. P. Kim, S. H. Blackmon, J. Rodriguez, H. Liu, C. Behrens, I. I. Wistuba, R. Minelli, K. L. Scott, J. Sanchez-Adams, F. Guilak, D. Pati, N. Thilaganathan, A. R. Burns, C. J. Creighton, E. D. Martinez, T. Zal, K. J. Grande-Allen, M. Yamauchi, J. M. Kurie, *J. Clin. Invest.* **2015**, *125*, 1147.
[74] Z. Mao, F. Nakamura, *Int. J. Mol. Sci.* **2020**, *21*, 2696.
[75] W. J. Sullivan, P. J. Mullen, E. W. Schmid, A. Flores, M. Momcilovic, M. S. Sharpley, D. Jelinek, A. E. Whiteley, M. B. Maxwell, B. R. Wilde, U. Banerjee, H. A. Coller, D. B. Shackelford, D. Braas, D. E. Ayer, T. Q. de Aguiar Vallim, W. E. Lowry, H. R. Christofk, *Cell* **2018**, *175*, 117.
[76] H. Nie, H. Ju, J. Fan, X. Shi, Y. Cheng, X. Cang, Z. Zheng, X. Duan, W. Yi, *Nat. Commun.* **2020**, *11*, 36.
[77] Y. Li, X. Y. Li, L. X. Li, R. C. Zhou, Y. Sikong, X. Gu, X. L. C. Zuo, *Front. Cell Dev. Biol.* **2020**, *8*, 559486.
[78] C. Li, Q. Chen, Y. Zhou, Y. Niu, X. Wang, X. Li, H. Zheng, T. Wei, L. Zhao, H. Gao, *FASEB J.* **2020**, *34*, 13333.
[79] J. Zhang, J. Yang, C. Lin, W. Liu, Y. Huo, M. Yang, S. H. Jiang, Y. Sun, R. Hua, *Theranostics* **2020**, *10*, 8400.
[80] Z. Chen, H. Bao, J. Long, P. Zhao, X. Hu, H. Wang, Y. Zhang, J. Yang, Q. Zhuge, L. Xia, *Cancers (Basel)* **2023**, *15*, 1594.
[81] J. Li, Y. He, Z. Tan, J. Lu, L. Li, X. Song, F. Shi, L. Xie, S. You, X. Luo, N. Li, Y. Li, X. Liu, M. Tang, X. Weng, W. Yi, J. Fan, J. Zhou, G. Qiang, S. J. Qiu, W. Wu, A. M. Bode, Y. Cao, *Theranostics* **2018**, *8*, 4050.
[82] H. M. Holden, I. Rayment, J. B. Thoden, *J. Biol. Chem.* **2003**, *278*, 43885.
[83] F. M. Buffa, A. L. Harris, C. M. West, C. J. Miller, *Br. J. Cancer* **2010**, *103*, 1136.
[84] G. R. You, J. T. Chang, H. F. Li, A. J. Cheng, *Cells* **2022**, *11*, 1581.
[85] R. G. Aktas, M. Karski, B. Issac, L. Sun, S. Rockowitz, P. Sliz, K. Vakili, *Cells* **2022**, *11*, 3797.
[86] A. S. Garcia Moreno, M. E. Guicciardi, A. Q. Wixom, E. Jessen, J. Yang, S. I. Ilyas, J. K. Bianchi, F. Pinto e Vairo, K. N. Lazaridis, G. J. Gores, *Res. Sq.* **2023**, *8*.
[87] V. Joshi, S. R. Lakhani, A. E. McCart Reed, *Cancers* **2022**, *14*.
[88] S. K. Kachhap, D. Faith, D. Z. Qian, S. Shabbeer, N. L. Galloway, R. Pili, S. R. Denmeade, A. M. DeMarzo, M. A. Carducci, *PLoS One* **2007**, *2*, 844.
[89] B. N. G. Giepmans, S. C. D. van IJzendoorn, *Biochim. et Biophys. Acta – Biomembranes* **2009**, *1788*, 820.
[90] C. J. Wu, P. Mannan, M. Lu, M. C. Udey, *J. Biol. Chem.* **2013**, *288*, 12253.
[91] K. C. Liu, D. T. Jacobs, B. D. Dunn, A. S. Fanning, R. E. Cheney, *Mol. Biol. Cell* **2012**, *23*, 1675.
[92] E. Nielsen, F. Severin, J. M. Backer, A. A. Hyman, M. Zerial, *Nat. Cell Biol.* **1999**, *1*, 376.
[93] Y.-T. Wu, S.-B. Wu, Y.-H. Wei, *Curr. Pharm. Des.* **2014**, *20*, 5510.
[94] A. Liberzon, C. Birger, H. Thorvaldsdóttir, M. Ghandi, J. P. Mesirov, P. Tamayo, *Cell Syst.* **2015**, *1*, 417.
[95] Y. Sato, K. Harada, K. Itatsu, H. Ikeda, Y. Kakuda, S. Shimomura, X. S. Ren, N. Yoneda, M. Sasaki, Y. Nakanuma, *Am. J. Pathol.* **2010**, *177*, 141.
[96] Z. Wang, J. Faria, L. J. W. van der Laan, L. C. Penning, R. Masereeuw, B. Spee, *Front. Bioeng. Biotechnol.* **2022**, *10*, 868857.
[97] E. Mazari-Arrighi, D. Ayollo, W. Farhat, A. Marret, E. Gontran, P. Dupuis-Williams, J. Larghero, F. Chatelain, A. Fuchs, *Biomaterials* **2021**, *279*, 121207.
[98] M. A. Odenwald, W. Choi, A. Buckley, N. Shashikanth, N. E. Joseph, Y. Wang, M. H. Warren, M. M. Buschmann, R. Pavlyuk, J. Hildebrand, B. Margolis, A. S. Fanning, J. R. Turner, *J. Cell Sci.* **2017**, *130*, 243.
[99] F. Sampaziotis, M. Cardoso de Brito, P. Madrigal, A. Bertero, K. Saeb-Parsy, F. A. C. Soares, E. Schrumpf, E. Melum, T. H. Karlsen, J. A. Bradley, W. T. H. Gelson, S. Davies, A. Baker, A. Kaser, G. J. Alexander, N. R. F. Hannan, L. Vallier, *Nat. Biotechnol.* **2015**, *33*, 845.
[100] A. R. Concepcion, M. Lopez, A. Ardura-Fabregat, J. F. Medina, *Front. Physiol.* **2014**, *4 JAN*, 413.
[101] C. He, Z. Yang, Y. Jin, X. Qi, J. Chu, X. Deng, *Front. Physiol.* **2018**, *9*.
[102] W. P. Bandura, A. Arbulu, *Am. Surg.* **1961**, *27*, 518.
[103] N. A. Gómez, L. R. Alvarez, A. Mite, J. P. Andrade, J. R. Alvarez, P. E. Vargas, N. E. Tomalá, A. F. Vivas, J. A. Zapatier, *J. Gastrointest. Surg.* **2002**, *6*, 116.
[104] M. Christensen, H. B. Laursen, M. Rokkær, P. F. Jensen, Y. Yasuda, F. V. Mortensen, *J. Hepatobiliary. Pancreat. Surg.* **2005**, *12*, 231.
[105] M. Miyazawa, M. Aikawa, J. Takashima, H. Kobayashi, S. Ohnishi, Y. Ikada, *World J. Gastroenterol.* **2022**, *28*, 5707.
[106] Z. Wang, J. Faria, L. C. Penning, R. Masereeuw, B. Spee, *Tissue Eng. – Part C: Methods* **2021**, *27*, 59.
[107] Q. Smith, J. Bays, L. Li, H. Shareef, C. S. Chen, S. N. Bhatia, *Adv. Sci.* **2022**, *9*, 1.
[108] Y. Du, G. Khandekar, J. Llewellyn, W. Polacheck, C. S. Chen, R. G. Wells, *Hepatology* **2020**, *71*, 1350.
[109] A. Funfak, L. Bouzhir, E. Gontran, N. Minier, P. Dupuis-Williams, S. Gobaa, *Front. Bioeng. Biotechnol.* **2019**, *7*, 417.
[110] P. L. Lewis, J. Su, M. Yan, F. Meng, S. S. Glaser, G. D. Alpini, R. M. Green, B. Sosa-Pineda, R. N. Shah, *Sci. Rep.* **2023**, *13*, 923.
[111] I. D. Gaudet, D. I. Shreiber, *Biointerphases* **2012**, *7*, 1.
[112] G. C. J. Lindberg, K. S. Lim, B. G. Soliman, A. Nguyen, G. J. Hooper, R. J. Narayan, T. B. F. Woodfield, *Appl. Phys. Rev.* **2021**, *8*.
[113] M. Klak, M. Gomółka, T. Dobrzański, G. Tymicki, P. Cywoniuk, P. Kowalska, K. Kosowska, T. Bryniarski, A. Berman, A. Dobrzyń, J. Idaszek, W. Święszkowski, M. Wszoła, *PLoS One* **2020**, *15*, 0235052.
[114] G. Holliman, D. Lowe, H. Cohen, S. Felton, K. Raj, *Sci. Rep.* **2017**, *7*, 11105.

[115] O. Gag, Ş. Dinu, H. Manea, I. Marcovici, I. Pînzaru, R. Popovici, Z. Crăiniceanu, Z. Gyori, G. Iovănescu, S. Chiriac, *Life* **2023**, *13*, 1144.
[116] M. Abedalwafa, F. Wang, L. Wang, C. Li, *Rev. Adv. Mater. Sci.* **2013**, *34*, 123.
[117] J. Keefe, L. Wauk, S. Chu, F. DeLustro, *Clin. Mater.* **1992**, *9*, 155.
[118] C. Yang, P. J. Hillas, J. A. Báez, M. Nokelainen, J. Balan, J. Tang, R. Spiro, J. W. Polarek, *BioDrugs* **2004**, *18*, 103.
[119] N. Dianat, H. Dubois-Pot-Schneider, C. Steichen, C. Desterke, P. Leclerc, A. Raveux, L. Combettes, A. Weber, A. Corlu, A. Dubart-Kupperschmitt, *Hepatology* **2014**, *60*, 700.
[120] X. Wang, X. Liu, K. Li, W. Liu, Y. Wang, S. Ji, Z. Gao, J. Ren, T. Hai, L. Hui, X. Zheng, Q. Gu, *Adv. Mater.* **2025**.
[121] A. F. Peery, S. D. Crockett, C. C. Murphy, J. L. Lund, E. S. Dellon, J. L. Williams, E. T. Jensen, N. J. Shaheen, A. S. Barritt, S. R. Lieber, B. Kochar, E. L. Barnes, Y. C. Fan, V. Pate, J. Galanko, T. H. Baron, R. S. Sandler, *Gastroenterology* **2018**, *156*, 254.
[122] X. Liu, J. Yan, J. Liu, Y. Wang, J. Yin, J. Fu, *Biofabrication* **2021**, *13*.
[123] A. D'Amore, J. A. Stella, W. R. Wagner, M. S. Sacks, *Biomaterials* **2010**, *31*, 5345.
[124] Q. Li, P. Wang, C. Liu, F. Liu, H. Zhao, Y. Guo, G. Zhao, *J. Mech. Behav. Biomed. Mater.* **2022**, *136*, 105494.
[125] L. Dong, S. J. Wang, X. R. Zhao, Y. F. Zhu, J. K. Yu, *Sci. Rep.* **2017**, *7*, 13412.
[126] Z. Li, B. Yuan, X. Dong, L. Duan, H. Tian, C. He, X. Chen, *RSC Adv.* **2015**, *5*, 94248.
[127] M. G. Francipane, B. Han, L. Oxburgh, S. Sims-Lucas, Z. Li, E. Lagasse, *J. Tissue Eng. Regener. Med.* **2019**, *13*, 1724.
[128] T. Dębski, J. Wysocki, K. Siennicka, J. Jaroszewicz, K. Szlązak, W. Święszkowski, Z. Pojda, *Materials (Basel)*. **2022**, *15*, 1732.
[129] M. G. Francipane, B. Han, E. Lagasse, *Am. J. Pathol.* **2020**, *190*, 252.
[130] J. R. Wiśniewski, A. Zougman, N. Nagaraj, M. Mann, *Nat. Methods* **2009**, *6*, 359.
[131] J. Rappsilber, M. Mann, Y. Ishihama, *Nat. Protoc.* **2007**, *2*, 1896.